arXiv:2410.05397v1 [astro-ph.GA] 7 Oct 2024

Polycyclic Aromatic Hydrocarbon and CO (2-1) Emission at $50-150$ pc Scales in 66 Nearby Galaxies

Ryan Chown,[1] Adam K. Leroy,[1,2] Karin Sandstrom,[3] Jérémy Chastenet,[4] Jessica Sutter,[5,3] Eric W. Koch,[6] Hannah B. Koziol,[3] Lukas Neumann,[7] Jiayi Sun,[8] Thomas G. Williams,[9] Dalya Baron,[10,11] Gagandeep S. Anand,[12] Ashley. T. Barnes,[13] Zein Bazzi,[7] Francesco Belfiore,[14] Alberto Bolatto,[15] Médéric Boquien,[16] Yixian Cao,[17] Mélanie Chevance,[18] Dario Colombo,[7] Daniel A. Dale,[19] Oleg V. Egorov,[20] Cosima Eibensteiner,[21,*] Eric Emsellem,[13,22] Hamid Hassani,[23] Jonathan D. Henshaw,[24,25] Hao He,[7] Jaeyeon Kim,[11] Kathryn Kreckel,[20] Sharon E. Meidt,[4] Eric J. Murphy,[21] Elias K. Oakes,[26] Eve C. Ostriker,[8,27] Hsi-An Pan,[28] Debosmita Pathak,[1,2] Erik Rosolowsky,[23] Sumit K. Sarbadhicary,[1,2,29] Eva Schinnerer,[25] and Yu-Hsuan Teng[15]

[1]*Department of Astronomy, The Ohio State University, 140 West 18th Avenue, Columbus, OH 43210, USA*
[2]*Center for Cosmology and Astroparticle Physics (CCAPP), 191 West Woodruff Avenue, Columbus, OH 43210, USA*
[3]*Department of Astronomy & Astrophysics, University of California, San Diego, 9500 Gilman Dr., La Jolla, CA 92093, USA*
[4]*Sterrenkundig Observatorium, Universiteit Gent, Krijgslaan 281 S9, B-9000 Gent, Belgium*
[5]*Whitman College, 345 Boyer Avenue, Walla Walla, WA 99362, USA*
[6]*Center for Astrophysics | Harvard & Smithsonian, 60 Garden St., 02138 Cambridge, MA, USA*
[7]*Argelander-Institut für Astronomie, University of Bonn, Auf dem Hügel 71, 53121 Bonn, Germany*
[8]*Department of Astrophysical Sciences, Princeton University, Princeton, NJ 08544, USA*
[9]*Sub-department of Astrophysics, Department of Physics, University of Oxford, Keble Road, Oxford OX1 3RH, UK*
[10]*The Observatories of the Carnegie Institution for Science. 813 Santa Barbara Street, Pasadena, CA 91101, USA*
[11]*Kavli Institute for Particle Astrophysics & Cosmology (KIPAC), Stanford University, CA 94305, USA*
[12]*Space Telescope Science Institute, 3700 San Martin Drive, Baltimore, MD 21218, USA*
[13]*European Southern Observatory (ESO), Karl-Schwarzschild-Straße 2, 85748 Garching, Germany*
[14]*INAF — Osservatorio Astrofisico di Arcetri, Largo E. Fermi 5, I-50125, Florence, Italy*
[15]*Department of Astronomy and Joint Space-Science Institute, University of Maryland, College Park, MD 20742, USA*
[16]*Université Côte d'Azur, Observatoire de la Côte d'Azur, CNRS, Laboratoire Lagrange, 06000, Nice, France*
[17]*Max-Planck-Institut für Extraterrestrische Physik (MPE), Giessenbachstr. 1, D-85748 Garching, Germany*
[18]*Universität Heidelberg, Zentrum für Astronomie, Institut für Theoretische Astrophysik, Albert-Ueberle-Str 2, D-69120 Heidelberg, Germany, Cosmic Origins Of Life (COOL) Research DAO, coolresearch.io*
[19]*Department of Physics and Astronomy, University of Wyoming, Laramie, WY 82071, USA*
[20]*Astronomisches Rechen-Institut, Zentrum für Astronomie der Universität Heidelberg, Mönchhofstr. 12-14, D-69120 Heidelberg, Germany*
[21]*National Radio Astronomy Observatory, Charlottesville, VA, USA*
[22]*Univ Lyon, Univ Lyon 1, ENS de Lyon, CNRS, Centre de Recherche Astrophysique de Lyon UMR5574, F-69230 Saint-Genis-Laval, France*
[23]*Dept. of Physics, University of Alberta, 4-183 CCIS, Edmonton, Alberta, T6G 2E1, Canada*
[24]*Astrophysics Research Institute, Liverpool John Moores University, 146 Brownlow Hill, Liverpool L3 5RF, UK*
[25]*Max-Planck-Institut für Astronomie, Königstuhl 17, D-69117, Heidelberg, Germany*
[26]*Department of Physics, University of Connecticut, 196A Auditorium Road, Storrs, CT 06269, USA*
[27]*Institute for Advanced Study, 1 Einstein Drive, Princeton, NJ 08540, USA*
[28]*Department of Physics, Tamkang University, No.151, Yingzhuan Road, Tamsui District, New Taipei City 251301, Taiwan*
[29]*Department of Physics and Astronomy, The Johns Hopkins University, Baltimore, MD 21218, USA*

ABSTRACT

Combining Atacama Large Millimeter/sub-millimeter Array CO(2-1) mapping and JWST near- and mid-infrared imaging, we characterize the relationship between CO(2-1) and polycyclic aromatic hydrocarbon (PAH) emission at ≈ 100 pc resolution in 66 nearby star-forming galaxies, expanding the sample size from previous ≈ 100 pc resolution studies by more than an order of magnitude. Focusing on regions of galaxies where most of the gas is likely to be molecular, we find strong correlations between

Corresponding author: Ryan Chown
rchown53@gmail.com

CO(2-1) and 3.3 μm, 7.7μm, and 11.3 μm PAH emission, estimated from JWST's F335M, F770W, and F1130W filters. We derive power law relations between CO(2-1) and PAH emission, which have indices in the range 0.8−1.2, implying relatively weak variations in the observed CO-to-PAH ratios across the regions that we study. We find that CO-to-PAH ratios and scaling relationships near H II regions are similar to those in diffuse sight lines. The main difference between the two types of regions is that sight lines near H II regions show higher intensities in all tracers. Galaxy centers, on the other hand, show higher overall intensities and enhanced CO-to-PAH ratios compared to galaxy disks. Individual galaxies show 0.19 dex scatter in the normalization of CO at fixed I_{PAH}, and this normalization anti-correlates with specific star formation rate (SFR/$M_{\star}$) and correlates with stellar mass. We provide a prescription that accounts for these galaxy-to-galaxy variations and represents our best current empirical predictor to estimate CO(2-1) intensity from PAH emission, which allows one to take advantage of JWST's excellent sensitivity and resolution to trace cold gas.

Keywords: Interstellar medium (847), Dust continuum emission (412), CO line emission (462), Disk galaxies (391), Dust nebulae (413), Extragalactic astronomy (506)

1. INTRODUCTION

Broad emission features at 3.3, 6.2, 7.7, 8.6, 11.2, and 12.7 μm, attributed to the stretching and bending modes of polycyclic aromatic hydrocarbons (PAHs; Puget & Leger 1989; Leger & Puget 1984; Allamandola et al. 1989; Tielens 2008), dominate the near- and mid-infrared (NIR and MIR) luminosities of star-forming galaxies (e.g., Smith et al. 2007; Tielens 2008; Galliano et al. 2018). Emission from PAHs has been used to trace the star formation rate (Peeters et al. 2004; Calzetti et al. 2007; Belfiore et al. 2023), interstellar radiation field, and PAH abundance (e.g., Draine et al. 2007; Kennicutt & Evans 2012; Whitcomb et al. 2023a; Baron et al. 2024; Sutter et al. 2024). At large scales (from a few kpc to integrated galaxies), PAH emission also shows a close correspondence with CO emission, exhibiting strong correlations and nearly linear scaling relations between PAH and CO intensity over three orders of magnitude (see Regan et al. 2004; Gao et al. 2019; Chown et al. 2021; Gao et al. 2022; Leroy et al. 2021, 2023a; Whitcomb et al. 2023a). CO emission traces the molecular gas in galaxies (e.g., Bolatto et al. 2013), and this has led to the suggestion that PAH emission may be used as a quantitative tracer of the interstellar medium (ISM), specifically molecular gas in star-forming galaxies. This prospect is particularly exciting because the widespread availability of maps tracing PAH emission from *WISE*, *Spitzer*, and now JWST, means that high-resolution, high-sensitivity maps of the atomic and molecular ISM could potentially be produced from every image of PAH emission obtained using these telescopes. In principle this could be done to higher redshifts than can be ac-

cessed with CO observations. Furthermore, the upcoming Spectro-Photometer for the History of the Universe, Epoch of Reionization and Ices Explorer satellite (SPHEREx, Doré et al. 2018), which will provide full-sky spectral maps of PAH emission, could also in principle be used to make maps of the atomic and molecular ISM across all nearby galaxies.

Initial JWST imaging of nearby galaxies supports the idea that PAH emission may act as a cold, dense ISM tracer. JWST images using PAH-dominated filters resemble sharper, more sensitive versions of Atacama Large Millimeter/sub-millimeter Array (ALMA) CO maps for the same galaxies (Leroy et al. 2023b; Sandstrom et al. 2023a). These analyses showed an excellent quantitative correspondence between CO (2-1) and emission in the F770W and F1130W filters at $\approx$ 100 pc scales (Leroy et al. 2023a), even suggesting that the PAH emission traces lower-density ISM emission into the H I-dominated parts of the ISM (Sandstrom et al. 2023a). However, these first studies focused on only four galaxies, and so the general relationship between CO and PAH emission at these 50-150 pc scales (similar to the sizes of molecular clouds, or "cloud scales") was not statistically robust. Fortunately, over its first two cycles of operations, JWST has nearly completed an extensive census of NIR and MIR PAH emission from 74 local ($D \lesssim 20$ Mpc) galaxies as part of the Physics at High Angular Resolution in Nearby Galaxies Survey (PHANGS) Cycle 1 and Cycle 2 treasuries. In addition to 0.03″ to 0.8″ ($\approx$ 15 to 120 pc) resolution JWST images, all of these galaxies also have $\approx$ 1″ ($\approx$ 50 to 150 pc) resolution CO (2-1) imaging from ALMA (Leroy et al. 2021).

In this paper, the first to take full advantage of the combined PHANGS-JWST Cycle 1 and 2 surveys, we

* Jansky Fellow of the National Radio Astronomy Observatory

use this large new set of ALMA and JWST data to make quantitative comparisons between CO(2-1) and PAH emission traced using JWST's F770W, F335M, and F1130W filters. We consider the 66 nearby galaxies with current in-hand JWST and high-quality ALMA observations, and address the following questions:

1. What are the median and scatter in the CO(2-1)/PAH band ratios across a representative sample of nearby star-forming galaxies at molecular cloud scales (50 to 150 pc)? What are the correlation strengths and best-fit parameters for the CO(2-1) vs. PAH power law scaling relationships?

2. Are there significant differences between the correlations measured for galaxy centers and galaxy disks, or when contrasting emission near H II regions with diffuse emission? Such variations might be expected given the different distributions of MIR intensity from these regions (Pathak et al. 2024) and the observation of systematic suppression of PAH emission from inside H II regions (Pety et al. 2005; Lebouteiller et al. 2007; Compiègne et al. 2008; Chastenet et al. 2023a; Egorov et al. 2023; Sutter et al. 2024).

3. How does the observed CO(2-1)-PAH relationship vary from galaxy to galaxy? Does it change as a function of parameters that also correlate with dust and PAH abundances or the interstellar radiation field? Or do these factors affect CO emission in a similar way to PAH emission, suppressing the impacts of environmental variations on the correlation?

We describe our expectations for this work in §2, our approach in §3, present our results in §4, and discuss and summarize our conclusions in §5 and §6. Throughout, we focus on F770W emission because it has the widest availability out of all of the PAH bands that we consider, in terms of the total number of galaxies observed and total area mapped.

2. EXPECTATIONS

Throughout the analysis, we will reference the expectation for emission from stochastically-heated PAHs subjected to a scaled version of the local interstellar radiation field and mixed with an ISM consisting of mostly molecular gas (e.g., Draine & Li 2007; Draine 2011; Compiègne et al. 2010). To first order we expect

$$I_{\rm PAH} \propto {\rm DGR} \times q_{\rm PAH} \times N_{\rm H_2} \times U \quad (1)$$
$$\propto ({\rm DGR} \times q_{\rm PAH} \times X_{\rm CO} \times U)\, I_{\rm CO},$$

where $I_{\rm PAH}$ and $I_{\rm CO}$ are the observed intensities of PAH and CO emission respectively, DGR is the dust-to-gas mass ratio, $q_{\rm PAH}$ is the PAH-to-dust mass fraction, U is the strength of the interstellar radiation field relative to that in the Solar neighborhood ($q_{\rm PAH}$ and U are defined in Draine et al. 2007), and $X_{\rm CO}$ is the CO-to-H_2 conversion factor.

This equation indicates why we expect a scaling relation in the first place. It also indicates the factors that might lead to environmental variations in the $I_{\rm CO}/I_{\rm PAH}$ ratio, and non-linearities in the observed scaling relations, e.g. when $U \gtrsim 10^3$ (for more discussion see Draine & Li 2007; Leroy et al. 2023a,b; Sandstrom et al. 2023a). For example, to first order, U is proportional to the local unextinguished $\Sigma_{\rm FUV} \propto \Sigma_{\rm SFR}$ (e.g., see recent simulations by Linzer et al. 2024), and so we expect PAH emission to be brighter where local star formation activity is more intense (though bear in mind the destruction of PAHs in H II regions mentioned above). We return to this expected correlation between $I_{\rm PAH}/I_{\rm CO}$ and star formation activity in §4.3. The hardness of the radiation field, variations in the dust-to-gas ratio, and PAH abundance variations may also be important, but in our selected molecular gas dominated regions of relatively massive galaxies, we mostly expect these to be second-order effects (see §4.3).

3. DATA AND METHODS

We analyze 66 galaxies that have both high-resolution ALMA CO (2-1) imaging and JWST imaging tracing PAH emission. Our targets are all part of the PHANGS surveys, and as such are relatively massive ($M_\star \gtrsim 10^{9.5}$ $M_\odot$), star-forming (SFR/$M_\star \gtrsim 10^{-11}$ yr^{-1}), and moderate inclination ($i \lesssim 70°$) galaxies within $D \lesssim 20$ Mpc (Leroy et al. 2021). The subset of 19 targets presented in Lee et al. (2023) and Williams et al. (2024) have both F1130W imaging and "nebular masks," which identify H II regions based on a morphological decomposition of the Hα emission observed by the Very Large Telescope's Multi-Unit Spectroscopic Explorer (VLT/MUSE Groves et al. 2023). The rest of the targets lack F1130W imaging and are not systematically covered with optical integral field spectroscopy, therefore lacking nebular masks. Both the JWST Cycle 1 and Cycle 2 data include the F335M filter but the continuum subtraction needed to isolate the PAH emission has only reached a science-ready state for the Cycle 1 data (§3.1). Therefore analyses that require nebular masks (§ 4.1) and/or F335M and/or F1130W are limited to our 19 Cycle 1 targets.

3.1. *JWST imaging of PAH emission*

We use JWST MIRI and NIRCam imaging of 19 galaxies from the PHANGS-JWST Cycle 1 Treasury (GO 2107, PI: J. Lee; Lee et al. 2023). These data cover the F335M, F770W, and F1130W bands, each of which captures a strong PAH feature (e.g., Tielens 2008). The F335M filter captures the prominent 3.3 μm feature, attributed to C–H stretching modes of small PAHs, while the F770W filter captures the 7.7 μm PAH feature, attributed to C–C stretching modes of larger PAHs, and the F1130W filter captures the 11.3 μm feature, attributed to C–H out-of-plane bending modes of larger PAHs (Tielens 2008). We also analyze 47/50 galaxies from the PHANGS-JWST Cycle 2 Treasury (GO 3707, PI: A. Leroy), which includes the F335M and F770W filters. Reduction for both data sets was done using the PHANGS-JWST pipeline (`pjpipe`[1]), following Williams et al. (2024). `pjpipe` is a wrapper on `jwst`[2], tailored to produce mosaics of images with extended emission. From the 50 available Cycle 2 galaxies, we remove NGC 3344 and NGC 1808 due to missing CO observations, and we remove NGC 1068 as the JWST flux anchoring for this galaxy is not science-ready. Removing these three galaxies leaves us with 66 galaxies in total.

The Rayleigh-Jeans tail of the stellar continuum contributes to F335M and F770W (more so for F335M). This contribution must be subtracted from the total surface brightnesses to obtain emission from PAHs. We calculate stellar-continuum-subtracted F770W surface brightness $I_{\mathrm{F770W}}^{\mathrm{PAH}}$ by subtracting F200W (Cycle 1) or F300M (Cycle 2) times a scaling factor (one factor per band) following Sutter et al. (2024). In our sample, the F770W stellar continuum correction (F770W$_\star$ = 0.22×F300M, or 0.12×F200W for Cycle 1) tends to be largest in the gas-poor, high stellar surface density inner regions of galaxies, including bars and bulges, which have high stellar-to-gas ratios. The coverage of F300M and F200W is smaller than that of F770W, and so for pixels without F300M or F200W data we subtract median(F770W$_\star$/F770W)×F770W, where the median (which is 2–10%, in agreement with Whitcomb et al. 2023b) is computed separately for each galaxy.

For F335M data, the stellar continuum subtraction is critical to any estimate of PAH emission (Sandstrom et al. 2023b). We use the continuum subtraction method defined by H. Koziol et al. (in preparation) based on Sandstrom et al. (2023b), where the F300M and F360M (for Cycle 1) are used to estimate continuum. We denote

the continuum-subtracted F335M surface brightness as $I_{\mathrm{F335M}}^{\mathrm{PAH}}$. A similar effort using the F300M is underway for Cycle 2 but not yet ready, and so our analysis of $I_{\mathrm{F335M}}^{\mathrm{PAH}}$ focused only on the Cycle 1 targets.

The F770W filter also captures emission from hot, very small dust grains, but this has a small effect (Baron et al. 2024, submitted, found that the 7.7 μm PAH emission is ≈ 5× brighter than the underlying continuum) and we do not subtract it off. In both data sets, we also masked out a few bright stars and background galaxies with elliptical apertures that cover all of the emission from these sources on top of the F770W images. We do not use any data within these apertures.

3.2. *ALMA CO(2-1)*

We use PHANGS–ALMA CO (2-1) observations, which are described in Leroy et al. (2021). All maps include short- and zero-spacing data and are expected to achieve full flux recovery. The native resolution is ≈ 1.0″, varying slightly from galaxy to galaxy. We use a noisy but uniform and high-completeness version of the CO (2-1) maps to ensure that > 90 % of the CO flux enters our analysis and that our mean trends will be unbiased by signal-to-noise based clipping of the CO data (see Leroy et al. 2023b). These "flat" maps are produced following Neumann et al. (2023) using a procedure analogous to spectral stacking. For each line of sight, we integrate over a fixed-width velocity window around the local mean velocity defined via either low-resolution CO emission, Hα emission, H I emission, or a model of the circular rotation, according to whichever yielded the most complete coverage and coherent reference velocity field for each galaxy. The velocity window is adapted to the disk-average line width of each individual galaxy and can vary from 20 to 200 km/s. We additionally ensure that all significant CO emission is included by combining the fixed-width velocity mask with the "strict" mask from Leroy et al. (2021). These "flat" masks will capture all of the CO emission along each line of sight and have well-defined noise, making them ideal to calculate the mean CO (2-1) intensity, I_{CO}, as a function of I_{PAH}.

3.3. *Environment masks*

We analyze how the CO-to-PAH correlations vary as functions of environment within galaxies, focusing on three specific environments: 1) galaxy centers; 2) regions outside galaxy centers with prominent nebular emission ("nebular regions"), which are ≳ 80% H II regions but also include a ∼ 10% contribution from supernova remnants (Li et al. 2024); and 3) regions outside of centers and not covered by the nebular region mask ("diffuse

---

[1] https://pjpipe.readthedocs.io/en/latest/
[2] https://jwst-pipeline.readthedocs.io/en/latest/index.html

regions"). Following Pathak et al. (2024) these three regions show distinct distributions of mid-IR intensity. These three regions likely show differences in radiation field strength and/or hardness, PAH abundance, H_2/H I ratio, and dust-to-gas ratio. Additionally, PAH emission is found to be systematically suppressed inside H II regions (Chastenet et al. 2023a; Egorov et al. 2023; Sutter et al. 2024; Chown et al. 2024).

We define galaxy centers using the masks in Querejeta et al. (2021), which are based on near-IR stellar morphology, and nebular regions following Santoro et al. (2022); Groves et al. (2023), which are based on ionized gas emission observed by the VLT/MUSE as part of the PHANGS-MUSE survey (Emsellem et al. 2022). The galaxy center masks are available for all targets, though only 53 of our targets have well-defined central regions. The rest of the targets do not have any pixels classified as being in a "center", and all of their pixels are included in the "disk" category. The nebular masks are available only for the 19 Cycle 1 targets, which restricts a subset of our analysis to that subsample. See Pathak et al. (2024) for further details on a similar application of these environment masks.

3.4. Analysis approach

To quantify the observed relationship between CO and PAH emission, we compile all measurements of individual pixels for all 66 galaxies into a single table, with columns for each NIR and MIR band (§3.1), CO(2-1) intensity (§3.2), and the values of each mask (§3.3). To avoid introducing systematic uncertainties, we analyze CO(2-1) intensities and do not adopt a CO-to-H_2 conversion factor. In Appendix B we describe how to use our results to estimate H_2 surface densities.

The CO (2-1) data have the coarsest angular resolution in this work. The CO resolution varies slightly from galaxy to galaxy. Over the range of distances of the galaxies in the sample, the working resolution for PHANGS–ALMA corresponds to median 98 pc with a $16-84\%$ range of $63-129$ pc (Table 15 in Leroy et al. 2021). Using webbpsf[3]-generated JWST PSFs, we convolve all JWST PAH images to share the same resolution of the corresponding CO (2-1) data following Aniano et al. (2011) and Williams et al. (2024). Then we define an astrometric grid with pixels 0.5 times the CO PSF FWHM in size so that approximately 4 pixels represent an independent measurement. We reproject the CO (2-1) intensity (in K km s^{-1}), JWST PAH intensity (in MJy sr^{-1}), and mask information onto this grid, noting

whether the majority of the area in each pixel corresponds to a galaxy center, a nebular region, or neither. We correct all intensities to face-on values by scaling by $\cos i$, where i is the galaxy inclination from Lang et al. (2020) and/or Leroy et al. (2021). The sample consists of nearly-face-on galaxies (median $\cos i = 0.7$), and so this correction does not have a large impact on our analysis.

PAH emission is also expected to emerge from dust mixed with atomic gas (e.g., see Sandstrom et al. 2023a). To avoid lines of sight where H I is expected to make up most of the ISM, we consider only regions that have inclination-corrected $I_{\mathrm{F770W}}^{\mathrm{PAH}} \geq 0.5$ MJy sr^{-1} (see Leroy et al. 2023a, for arguments about this specific value for "bright" emission). In Table 1 we report the percentages of flux or area that are classified as "bright" according to this criterion. Focusing on F770W-bright pixels means that we analyze the significant majority of flux in all bands across the sample. However, we do exclude a majority (48%) of the area in the maps outside galaxy centers and nebulae. Analysis of this faint, extended diffuse emission requires the inclusion of H I and will be the topic of future work.

The 3.3 μm PAH feature is $> 10\times$ fainter than the 7.7 and 11.3 μm ones (e.g., Chastenet et al. 2023a, Dale et al. in preparation), and the maps tend to be more limited by noise and systematic uncertainties related to continuum subtraction. As a result, we impose an additional threshold for analyzing the 3.3 μm emission, considering only lines of sight with $I_{\mathrm{F335M}}^{\mathrm{PAH}} > 0.1$ MJy sr^{-1}. This corresponds roughly to $I_{\mathrm{F770W}}^{\mathrm{PAH}} \gtrsim 2$ MJy sr^{-1} and was selected to catch the lines of sight where the 3.3 μm map yields robust detections at resolution matched to ALMA. Our analysis of F335M images is limited to lines of sight with surface brightness above this threshold.

Using the matched-resolution measurements, we analyze the correlation between CO (2-1) emission and emission in PAH-dominated JWST filters. For each MIR band X, we record the Spearman rank correlation coefficient (r), as well as the median and scatter in the ratio $I_{\mathrm{CO(2-1)}}/I_{\mathrm{X}}$. We then calculate a best-fit power law relating $I_{\mathrm{CO(2-1)}}$ to I_{X}. Because the PHANGS–ALMA CO maps are much less sensitive than the JWST F770W and F1130W maps at matched angular resolution (see Leroy et al. 2023b), we treat the mid-IR imaging as the independent (x) axis for this calculation. We construct logarithmically-spaced bins in I_{ν}^{X} and then compute the median and scatter, captured by the 16-84% range, of $I_{\mathrm{CO(2-1)}}$ within each bin.

---

[3] https://webbpsf.readthedocs.io/en/latest/

Table 1. Fraction of flux and area entering analysis

Quantity	All	Outside centers	Centers	Nebular	Diffuse
	%	%	%	%	%
F335M$_{\rm PAH}$[a]	99	99	99	99	100
F770W$_{\rm PAH}$[a]	91	89	99	99	88
F770W	89	88	99	98	87
F1130W	93	92	99	98	88
CO(2-1)	94	92	99	99	92
Area	52	52	95	82	48

[a]F335M$_{\rm PAH}$ and F770W$_{\rm PAH}$ refer to intensity in those filters after stellar continuum subtraction. After this correction, both filters are expected to be dominated by PAH emission (§3.4).

NOTE—Percentages of the flux or area in the full map captured in the subset of F770W-bright pixels with $I_{\rm F770W_{PAH}} \geq 0.5$ MJy sr^{-1} (see §3), by band and environment. Our analysis captures the majority of the flux in all bands, but only includes about half the total observed area.

We perform linear regression on these binned measurements[4] using `linmix`[5] a hierarchical Bayesian method described in Kelly (2007). It performs a linear regression of y on x while incorporating measurement errors in both variables. We model the CO-vs-PAH emission relationship as

$$\log_{10} I_{\rm CO(2-1)} = m(\log_{10} I_\nu^{\rm X} - x_0) + b, \qquad (2)$$

where the pivot $x_0 \equiv {\rm median}(x)$. Re-centering the fit at x_0 ensures minimal covariance between the best-fit m and b.

4. RESULTS

The top left panel of Figure 1 shows the correlation between CO (2-1) and star-subtracted F770W, $I_{\rm F770W}^{\rm PAH}$, for all F770W-bright pixels (§3.4) in all galaxies in our sample. Combining all 66 galaxies we find a strong correlation between CO (2-1) and starlight-subtracted F770W emission at $50-150$ pc resolution, with $r \approx 0.66$. Table 2 reports the best-fit relation derived from fitting the binned CO (2-1) as a function of $I_{\rm F770W}^{\rm PAH}$. Our measurements of the normalization $I_{\rm CO2-1}/I_{\rm F770W}^{\rm PAH} \approx 1.0$ K km s^{-1} (MJy sr^{-1})$^{-1}$ and the

---

[4] Because of the large number of individual pixels, the mean CO (2-1) intensity is detected at high signal-to-noise in all bins.

[5] https://linmix.readthedocs.io/en/latest/index.html

---

slope (Eq. 2) $m = 0.90 \pm 0.06$, agree reasonably well with previous work on much smaller samples or at lower resolution (Chown et al. 2021; Leroy et al. 2023a,a).

Our selection of bright pixels aims to include regions dominated by molecular gas. However, in the lowest $I_{\rm F770W}^{\rm PAH}$ bins ($1 \lesssim I_{\rm F770W}^{\rm PAH} \lesssim 30$ MJy sr^{-1}), we do see evidence of a slightly steeper relation, indicating lower CO-to-PAH ratios. This likely indicates a contribution of PAH emission associated with atomic gas (or perhaps CO-dark H$_2$) in these bins. At $I_{\rm F770W}^{\rm PAH} \lesssim 0.1$ MJy sr^{-1}, we would expect this to become the dominant effect because H I-dominated regions feature little-to-no CO emission while PAHs may remain present and excited there (Boulanger & Perault 1988). In the aforementioned low intensity regime of Figure 1, this would lead to a steeper, more scattered CO-vs-PAH relation, and likely a stronger correlation between H I column density and $I_{\rm F770W}^{\rm PAH}$.

At higher $I_{\rm F770W}^{\rm PAH}$ the correspondence between CO and PAH emission appears stronger, with only modest $\approx \pm 0.2$ dex scatter in the CO-to-PAH ratio in the high intensity (≈ 100 MJy sr^{-1}) bins. At lower $I_{\rm F770W}^{\rm PAH}$, which corresponds to most of the area, the scatter in CO at fixed $I_{\rm F770W}^{\rm PAH}$ appears somewhat higher, ± 0.5 dex. Much of this reflects the statistical noise in the PHANGS–ALMA CO maps, which often approaches $\approx \pm 1$ K km s^{-1} in the "flat" CO maps that we use. Our averaging approach recovers the median trend well, but this leads to a large scatter in the data in faint regions of each galaxy. We note that the noise is normally-distributed, which leads to asymmetric scatter when shown in log-space.

4.1. Nebular and diffuse regions

A number of studies have already demonstrated suppression of PAH emission, likely due to PAH destruction, within H II regions (e.g., Madden et al. 2006; Povich et al. 2007; Gordon et al. 2008; Montillaud et al. 2013; Chastenet et al. 2023a; Egorov et al. 2023; Pedrini et al. 2024; Sutter et al. 2024), while the intense radiation fields around H II regions also lead them to stand out as the brightest features in MIR maps of galaxy disks (Pathak et al. 2024). We note that at the physical resolution of PHANGS/JWST, PAH emission is reduced but still detected inside H II regions.

The top-right panel in Figure 1 separates sight lines in galaxy disks into those near H II regions and diffuse (i.e., all other) regions, and Table 2 presents our correlation analysis for these two regions separately. Perhaps surprisingly, we find median CO/F770W$_{\rm PAH}$ ratios in H II and diffuse regions to be quite similar, with H II regions exhibiting a ratio only ≈ 0.07 dex ($1.17\times$) lower

Table 2. Ratios, correlation, and scaling relations between PAH and CO (2-1) emission. Each section of the table reports results for a different data selection.

X	$N_{\rm gal}$	$N_{\rm pix}$[a]	$\log_{10} {\rm CO}/X$	r	b	m	x_0	σ[b]
				All pixels				
F335M$_{\rm PAH}$	19	77416	1.27 ± 0.38	0.60	1.30 ± 0.07	1.02 ± 0.10	0.05	0.44
F770W$_{\rm PAH}$	66	1902434	0.00 ± 0.33	0.66	1.38 ± 0.06	0.90 ± 0.06	1.44	0.43
F770W	66	2108986	-0.03 ± 0.33	0.67	1.31 ± 0.05	0.93 ± 0.05	1.39	0.44
F1130W	19	261827	-0.12 ± 0.37	0.62	1.13 ± 0.08	1.00 ± 0.08	1.28	0.44
				All pixels outside of centers				
F335M$_{\rm PAH}$	19	73559	1.25 ± 0.37	0.58	1.09 ± 0.07	0.89 ± 0.16	-0.10	0.43
F770W$_{\rm PAH}$	66	1871613	-0.00 ± 0.33	0.65	0.98 ± 0.07	0.88 ± 0.11	1.08	0.43
F770W	66	2077565	-0.03 ± 0.33	0.66	0.98 ± 0.07	0.87 ± 0.10	1.08	0.44
F1130W	19	256109	-0.13 ± 0.37	0.61	0.84 ± 0.09	1.00 ± 0.14	1.04	0.44
				All pixels in centers				
F335M$_{\rm PAH}$	15	3838	1.61 ± 0.36	0.75	1.59 ± 0.07	0.77 ± 0.09	0.05	0.44
F770W$_{\rm PAH}$	53	30814	0.18 ± 0.36	0.84	1.51 ± 0.06	0.81 ± 0.06	1.44	0.43
F770W	53	31414	0.12 ± 0.36	0.84	1.41 ± 0.06	0.86 ± 0.06	1.39	0.45
F1130W	15	5651	-0.05 ± 0.29	0.88	1.27 ± 0.08	0.95 ± 0.09	1.34	0.41
				All pixels in nebular regions (Cycle 1 only)				
F335M$_{\rm PAH}$	19	28398	1.19 ± 0.33	0.72	1.06 ± 0.07	0.95 ± 0.14	-0.10	0.38
F770W$_{\rm PAH}$	19	44643	-0.00 ± 0.35	0.77	0.91 ± 0.09	0.98 ± 0.13	0.94	0.39
F770W	19	46814	-0.01 ± 0.35	0.77	0.84 ± 0.09	0.98 ± 0.13	0.90	0.40
F1130W	19	46709	-0.17 ± 0.33	0.79	0.82 ± 0.09	1.01 ± 0.13	1.04	0.39
				All pixels in diffuse regions (Cycle 1 only)				
F335M$_{\rm PAH}$	19	45134	1.30 ± 0.40	0.47	0.87 ± 0.13	1.20 ± 0.42	-0.45	0.46
F770W$_{\rm PAH}$	19	184409	0.07 ± 0.39	0.52	0.70 ± 0.14	1.21 ± 0.30	0.66	0.47
F770W	19	208256	0.05 ± 0.39	0.52	0.65 ± 0.12	1.19 ± 0.27	0.65	0.47
F1130W	19	209396	-0.12 ± 0.38	0.54	0.68 ± 0.12	1.25 ± 0.23	0.80	0.46

[a] Pixels have size FWHM/2, so that there are four pixels per independent measurement.

[b] This scatter reflects the combined noise in the CO data, galaxy-to-galaxy scatter, and scatter about the fit within each galaxy. It is usually dominated by the noise in the CO data.

Note— Columns: X — JWST band compared to CO(2-1); $N_{\rm gal}$ — number of galaxies entering this analysis; $N_{\rm pix}$ — number of sightlines with $I_{\rm F770W}^{\rm PAH}$ entering correlation analysis; $\log_{10} {\rm CO}/X$ — $\log_{10}$ of median ratio of CO(2-1) in K km s^{-1} to intensity in MJy sr^{-1} in band X with error indicating the scatter in the ratio estimated from the median absolute deviation; r — rank correlation between CO(2-1) and intensity in band X for all sightlines; b, m, x_0 — best fit power law scaling parameters following Equation 2 relating CO(2-1) to intensity in band X; σ — rms scatter in dex of individual data about the best fit scaling relation, inferred via the median absolute deviation.
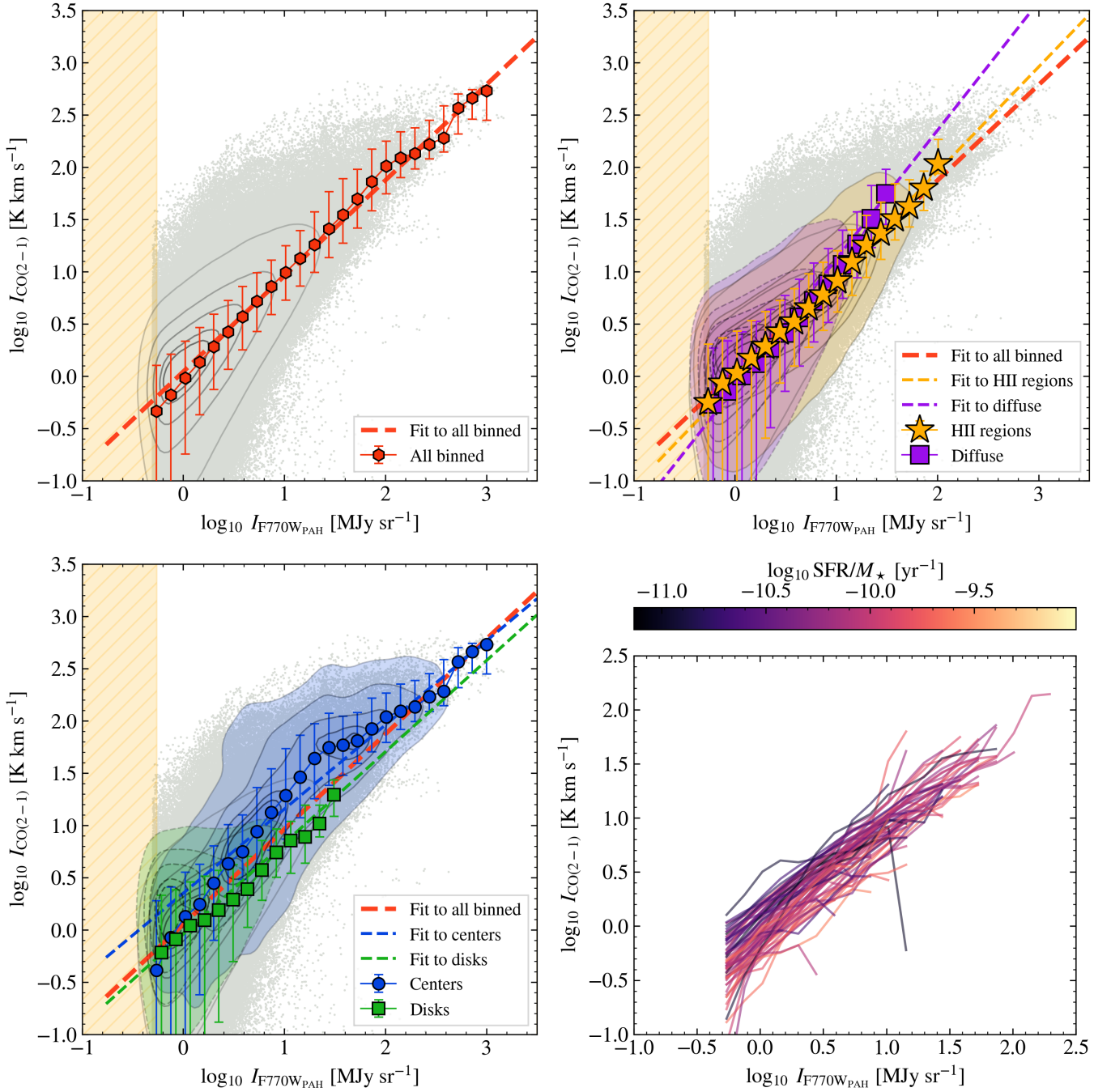
Figure 1. CO(2–1) and starlight continuum-subtracted F770W$_{\mathrm{PAH}}$ emission at ≈ 100 pc resolution in 66 nearby star-forming galaxies. *Top left:* All sight lines in our analysis (gray points) with data density contours enclosing the densest 15, 25, 50, 75, and 95% of the data points. The bins show the median and 16-84% range of CO(2-1) emission in logarithmically-spaced bins of $I_{\mathrm{PAH}}^{\mathrm{F770W}}$; treating the PAH emission as the independent variable allows us to average the noisier CO(2-1) data. The dashed line shows the best-fit power law describing these binned measurements (Table 2). *Top right:* As the top left panel but now separately plotting results for sight lines near H II regions (yellow, stars) and diffuse emission outside these regions (purple, squares). The two environments show similar CO-to-PAH ratios where they overlap, but the sight lines near H II regions show overall brighter intensities. *Bottom left:* As for the previous figures, but now separating galaxy centers (blue, circles) from disks (green, squares). Galaxy centers show brighter emission and higher CO-to-PAH ratios at the same $I_{\mathrm{F770W}}^{\mathrm{PAH}}$. *Bottom right:* Traces show binned results for each individual galaxy. The galaxies show overall similar CO(2-1) vs. F770W$_{\mathrm{PAH}}$ relations with moderate offsets from galaxy to galaxy. These offsets correlate with the integrated galaxy properties (see Figure 2, with the color bar indicating SFR/$M_\star$). See Table 2 for ratios and best fits for each panel.

than diffuse regions (i.e., PAHs are slightly brighter relatively to CO near H II regions). The correlation strength near H II regions appears stronger than in diffuse regions ($r \approx 0.8$ vs. $r \approx 0.5$), but this partially reflects that the sight lines near H II regions tend to be brighter, and so less affected by the high statistical noise in the CO maps. The slightly steeper relationship observed for the diffuse regions reflects that diffuse sight lines with $I_{\mathrm{F770W}}^{\mathrm{PAH}} \gtrsim 10$ MJy sr^{-1} show slightly elevated CO/PAH ratios compared to nebular regions with similar intensities, which may be due to preferential destruction of CO compared to PAHs in nebular regions. This preferential destruction may be related to recent work demonstrating that PAH emission is slightly more long-lived than CO emission in gas-poor regions (Kim et al. in preparation). Sight lines with $I_{\mathrm{F770W}}^{\mathrm{PAH}} \lesssim 10$ MJy sr^{-1} in Figure 1 show almost identical CO-to-PAH ratios for diffuse and nebular regions.

The similarity of the CO-vs-PAH relationship in diffuse and nebular regions likely results from the fact that the H II region masks that we use (from Groves et al. 2023) are based on data with coarse resolution (median 70 pc) compared to the actual size of most H II regions (e.g., see Barnes et al. 2022). As a result, these regions often include CO and PAH emission from ISM material projected towards, but not actually inside H II regions. The CO and PAH emission may come from the well-shielded material surrounding the H II regions. Sutter et al. (2024) discuss a scenario in which the Groves et al. (2023) regions contain a mixture of diffuse material and true H II regions to explain observed F770W/F2100W ratios. Resolved comparisons of high ($\lesssim 10$ pc) physical resolution Hα, Paα, CO, and MIR emission (e.g., Pedrini et al. 2024) should help test this hypothesis in the near future. Subtracting hot dust continuum emission from F770W, which we do not do, may also be important, since the filter still captures such emission in regions where PAHs have been destroyed to the point where their emission is not detectable.

4.2. *Centers and disks of galaxies*

Galaxy centers, especially bar-fed central molecular zones, differ from the disks of galaxies in ways that may also affect CO-to-PAH ratios. Galaxy centers exhibit some of the most intense star formation found in galaxies, with correspondingly high interstellar radiation fields, gas column and volume densities, and some host active galactic nuclei (e.g., Schinnerer et al. 2023, and see review in Schinnerer & Leroy 2024). As a result, CO in galaxy centers often exhibits broader line widths, lower opacity, and low X_{CO} (e.g., Bolatto et al. 2013; Teng et al. 2023).

The bottom-left panel of Figure 1 shows the CO-vs-PAH relationship separating sight lines towards galaxy centers compared to those in disks. Galaxy centers appear systematically brighter than disks in both CO and PAH emission, as expected from previous analyses of these galaxies (Sun et al. 2020; Pathak et al. 2024). Sight lines in galaxy centers also appear offset towards higher CO intensity compared to disks at matched $I_{\mathrm{F770W}}^{\mathrm{PAH}}$. On average the CO-to-PAH ratio is ≈ 0.18 dex ($\approx 60\%$) higher in galaxy centers compared to disks, and the median $I_{\mathrm{CO(2-1)}}$ in centers appear higher than that found for disks at fixed $I_{\mathrm{F770W}}^{\mathrm{PAH}}$.

We note one caveat here. The stellar continuum can also be bright in galaxy centers, and the starlight subtraction can become correspondingly more difficult (e.g., Sutter et al. 2024; Baron et al. 2024). If our standard correction oversubtracts the starlight from F770W in galaxy centers, then we might artificially underestimate F770W$_{\mathrm{PAH}}$. However, considering a similar situation, Baron et al. (2024) found that the range of plausible starlight SED variations is not sufficient to explain observed variations in PAH emission (there they consider F770W/F1130W). We also note that we find a similar contrast between disks and centers in the CO-to-F1130W ratio, where F1130W is less affected by starlight. Finally, we note that we do not subtract any hot dust continuum from F770W. Hot dust continuum is likely stronger in galaxy centers, implying that the CO-to-PAH ratio will be biased high.

A higher CO-to-PAH ratio in bright galactic centers may imply a large impact of X_{CO} on the measured ratio. A number of studies have shown that X_{CO} in galaxy centers can be 5–15 times lower than the standard Milky Way $X_{\mathrm{CO}} = 2 \times 10^{20}$ cm^{-2}/(K km s^{-1}), and $\approx 2\times$ lower than the galaxy mean on average (e.g., Sandstrom et al. 2013; Israel 2020; Teng et al. 2023; Chiang et al. 2024). Following Equation 1, centrally suppressed X_{CO} will lead to centrally enhanced CO-to-PAH ratios. On the other hand, the intense radiation fields expected in galaxy centers should increase PAH emission and decrease the CO-to-PAH ratio, unless PAH destruction occurs. There is some evidence for slightly lower q_{PAH} in galaxy centers (Chastenet et al. 2023b), but a general trend is not so clear. Metallicity and DGR tend to be highest in galaxy centers, which may also decrease the CO-to-PAH ratio (see Eq. 1). Considering that most of these effects would decrease CO-to-PAH, the enhancement seen in Figure 1 and Table 2 may indicate that X_{CO} represents the dominant effect, offsetting these other PAH-enhancing effects.
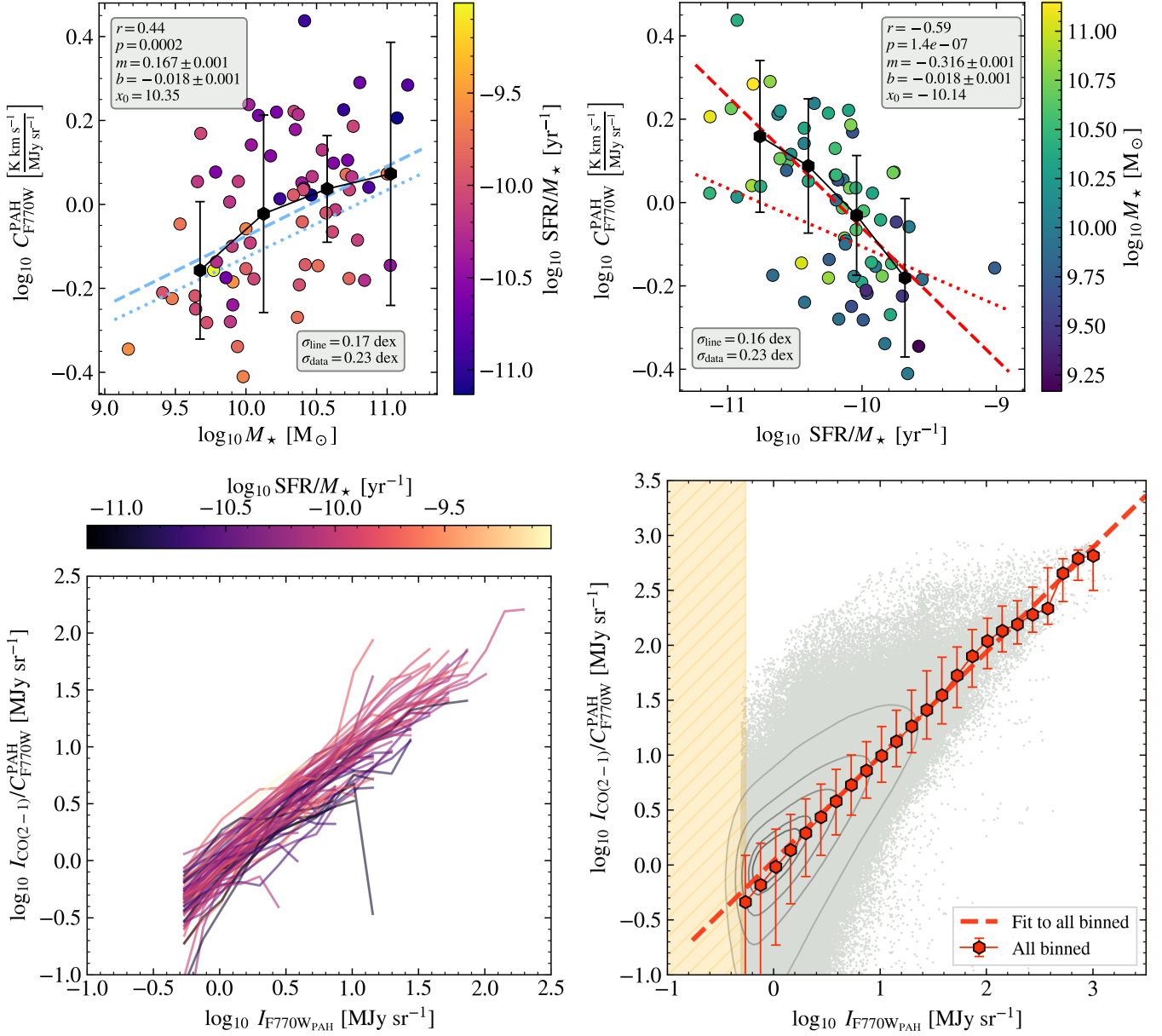
4.3. *Galaxy to galaxy variations*

Figure 2. Galaxy-to-galaxy variations in the CO(2–1) vs. F770W$_{\rm PAH}$ relationship. CO(2-1) at fixed PAH intensity for individual galaxies (see bottom left panel Fig. 1) as a function of (*left*) galaxy-integrated stellar mass, $M_\star$ and (*right*) specific star formation rate, SFR/$M_\star$. Spearman's r, p-value, the best-fit slope, intercept and pivot ($y = m(x - x_0) + b$) to all galaxies, the scatter about the best-fit relation (Eq. 3), and vertical scatter are all indicated. We observe a modest correlation between the CO-to-PAH ratio and $M_\star$ and a well-defined anti-correlation between the CO-to-PAH ratio and SFR/$M_\star$. The correlation with $M_\star$ may reflect increased contribution of PAH emission associated with CO-dark gas or atomic gas in low mass galaxies. The anti-correlation with SFR/$M_\star$ likely reflects a mixture of increased radiation field strength, suppression of $X_{\rm CO}$, and enhancement of R_{21} in high SFR/$M_\star$ galaxies, which appear to represent stronger effects than any $q_{\rm PAH}$. Scaled versions of the best-fit normalizations of $I_{\rm CO(2-1)}$ vs *WISE* 12 μm against stellar mass and SFR/$M_\star$ from Leroy et al. (2023a) are shown (dotted lines), showing similar trends.

So far, we have treated all galaxies together, separating sight lines into categories but not otherwise differentiating between targets. However, our sample spans a range of stellar mass ($M_\star$), star formation rate (SFR), metallicity, morphology, and more. These factors will influence U, DGR, q_{PAH}, and X_{CO} and so we might expect differences among the CO-PAH relationships for different galaxies (as in Chown et al. 2021). To explore the impact of these variations, the bottom-right panel of Figure 1 shows the CO-to-F770W relationship varies from galaxy to galaxy. The fits for individual galaxies are provided in Appendix A.

The bottom right panel of Figure 1 shows that individual galaxies exhibit strong CO-PAH correlations, mostly parallel to our best-fit overall relation. Broadly, the agreement among the 66 individual galaxies appears good, supporting the potential use of PAHs to trace CO. Specifically, the normalization of the CO-PAH relation scatters by ± 0.19 dex from galaxy to galaxy. Simply applying our best fit overall relation to an individual galaxy with no additional information can be expected to yield a map biased by a factor drawn from this galaxy-to-galaxy scatter.

In Figure 2, we test how these galaxy-to-galaxy offsets correlate with integrated galaxy properties. We compute the normalization of the best-fit CO(2-1) versus F770W$_{\mathrm{PAH}}$ power law for each galaxy, $C_{\mathrm{F770W}}^{\mathrm{PAH}}$, by performing a linear fit of $\log_{10} I_{\mathrm{CO(2-1)}}$ versus $\log_{10} I_{\mathrm{F770W}}^{\mathrm{PAH}}$ for each galaxy. $C_{\mathrm{F770W}}^{\mathrm{PAH}}$ is then given by the value of the best-fit relation at $I_{\mathrm{F770W}}^{\mathrm{PAH}} = 1$ MJy sr^{-1}. We plot $C_{\mathrm{F770W}}^{\mathrm{PAH}}$ against $M_\star$ and specific star formation rate (SFR/$M_\star$) (WISE+GALEX-based galaxy-integrated SFR and $M_\star$ are drawn from Leroy et al. 2021). Stellar mass correlates with the H$_2$/H I ratio, gas-phase metallicity, DGR, X_{CO} and more (e.g., Saintonge & Catinella 2022). Meanwhile, SFR/$M_\star$ anti-correlates with q_{PAH}, and correlates with the mean interstellar radiation field, $\bar{U}$ (Chastenet et al. 2024, accepted). Therefore following Equation 1 both parameters might be expected to impact the CO-to-PAH ratio. Correlations between the galaxy-integrated CO-to-12μm ratio (with the 12μm data from WISE) with star formation activity, stellar mass, and SFR/$M_\star$ have previously been observed (Chown et al. 2021; Leroy et al. 2023a).

Consistent with previous work we find a mild positive correlation between the CO/PAH ratio at fixed $I_{\mathrm{F770W}}^{\mathrm{PAH}}$ and $M_\star$ and an anti-correlation between the CO/PAH normalization and SFR/$M_\star$. As seen in the bottom right of Figure 1, the galaxy-to-galaxy offsets are thus not random but agree with physical expectations. The $\log_{10} C_{\mathrm{F770W}}^{\mathrm{PAH}}$ vs. $\log_{10}$SFR/$M_\star$ trend may indicate the

higher U associated with high SFR/$M_\star$ galaxies leads to stronger PAH emission, offsetting any suppression due to lower q_{PAH} at high SFR/$M_\star$. As mentioned in §2, the anti-correlation between $C_{\mathrm{F770W}}^{\mathrm{PAH}}$ and SFR/$M_\star$ is expected because the dust heating rate increases with SFR/$M_\star$. The $\log_{10} C_{\mathrm{F770W}}^{\mathrm{PAH}}$ vs $\log_{10} M_\star$ trend goes in the sense that galaxies with higher metallicity, DGR, and molecular-to-atomic gas ratios (e.g., Saintonge et al. 2017) show higher CO-to-PAH ratios. As a result, perhaps the low observed CO-to-PAH ratios seen in low $M_\star$ systems reflects that the PAH emission is coming from regions dominated by H I or CO-dark H$_2$ despite our selection of only bright emission.

We also checked for correlations with distance and inclination to test how orientation and resolution might bias our results. We found that the normalization is uncorrelated with distance ($r = -0.04, p = 0.78$), and weakly correlated with $\cos i$ ($r = 0.24, p = 0.06$). Variations in $\cos i$ from galaxy to galaxy simply slide the data points parallel to a 1:1 relation. Since the best-fit slopes of CO(2-1) vs. PAH emission for each galaxy and for the sample as a whole are within a few percent of 1.0, and furthermore that the sample covers a range of inclinations across the full $M_\star$ range, it is understandable that $\cos i$ does not have a significant effect.

We fit functional forms to the two trends and note the SFR/$M_\star$ as the stronger, clearer trend. These predict the normalization of the CO vs. PAH relation as functions of galaxy-integrated $M_\star$ or SFR/$M_\star$

$$\log_{10} C_{\mathrm{F770W}}^{\mathrm{PAH}} = 0.167 \pm 0.001 \quad (\log_{10} M_\star - 10.35)$$
$$-0.018 \pm 0.001, \quad (3)$$
$$\log_{10} C_{\mathrm{F770W}}^{\mathrm{PAH}} = -0.316 \pm 0.001 (\log_{10} \mathrm{SFR}/M_\star + 10.14)$$
$$-0.018 \pm 0.001. \quad (4)$$

In the bottom panels of Figure 2 we normalize the data from each galaxy by the values predicted by this fit, aiming to remove galaxy-to-galaxy scatter. Then we re-fit the relation to all data (lower right panel) and find

$$\log_{10} I_{\mathrm{CO(2-1)}} = (0.95 \pm 0.06)(x - 1.44) + (1.40 \pm 0.06), \quad (5)$$

with scatter $\sigma = 0.43$ dex, where $x \equiv \log_{10} I_{\mathrm{F770W}}^{\mathrm{PAH}} - \log_{10} C_{\mathrm{F770W}}^{\mathrm{PAH}}$. We describe how to use these prescriptions in Appendix B.

4.4. CO (2-1) and PAH emission for other bands

So far we have focused only on the correlation between CO(2-1) and F770W$_{\mathrm{PAH}}$. Do the other PAH-tracing filters show similar correlations? In Figure 3 we show CO versus F335M$_{\mathrm{PAH}}$ and versus F1130W for our 19 Cycle 1 targets. The median CO/PAH ratios, fits and statistics for these bands are shown in Table 2. The corre-
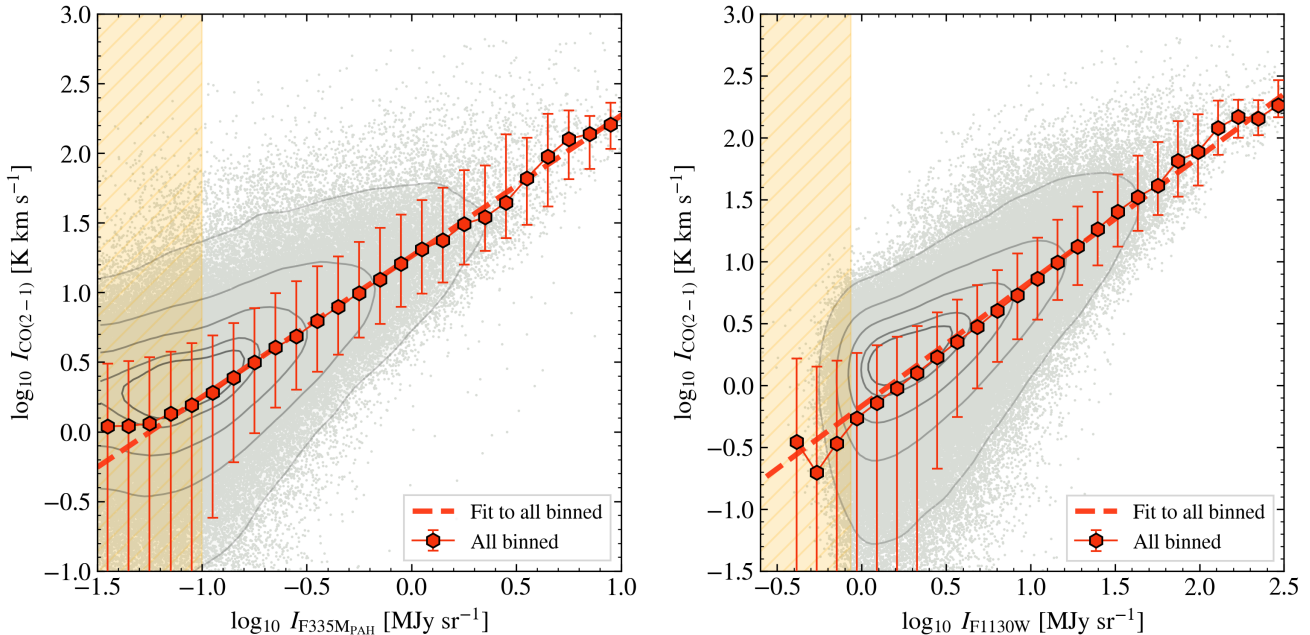
Figure 3. CO(2–1) intensity as functions of 3.3 μm and 11.3 μm PAH intensity. As Figure 1, but now showing PAH intensity captured by (*left*) the F335M filter capturing the 3.3 μm PAH feature (after continuum subtraction following H. Koziol et al. in preparation) and (*right*) the F1130W filter capturing the 11.3 μm PAH feature. The relationship between CO(2-1) and these bands resembles that which we observe for F770W$_{\rm PAH}$ in Figure 1, though the specifics of the fits differ (Table 2). Of note, the F335M$_{\rm PAH}$ feature has a lower intensity than the others and extracting it from imaging depends critically on stellar continuum subtraction, but the shorter wavelength means that the band offers even higher resolution compared to the other features (see Sandstrom et al. 2023b).

lation remains strong in both of these bands, and the best fit binned CO-PAH slopes are also very close to linear for the 3.3 μm and 11.3 μm features. Of the three PAH bands, F335M$_{\rm PAH}$ is the faintest (Chastenet et al. 2023b; Sandstrom et al. 2023b), and therefore shows the largest CO-to-PAH ratios ($10^{1.27}$ K km s^{-1}/(MJy sr^{-1}) vs. $10^{0.00}$ for F770W$_{\rm PAH}$ and $10^{-0.12}$ for F1130W considering all data, top rows of Table 2).

These three PAH bands (3.3, 7.7, and 11.3 μm) are dominated by different species of the PAH population – smaller, neutral PAHs for 3.3 μm, ionized PAHs for a range of sizes for 7.7 μm, and larger, mainly neutral PAHs for 11.3 μm. Their intensity ratios also respond to changes in the interstellar radiation field spectrum (e.g., Maragkoudakis et al. 2020; Draine et al. 2021). All three bands yield reasonable first-order estimators of CO intensity, but we would not expect all three to show identical or even equally good correlations with CO. We anticipate that future work will explore optimal combinations of bands to trace CO (and H$_2$) and examine the impact of conditions in the molecular gas on PAH band ratios.

From a practical perspective, each band has unique advantages. The F770W band traces the brightest PAH feature and is available now for > 70 nearby galaxies.

The F335M filter offers even sharper resolution but harbors the fainter 3.4 μm PAH feature, the Pfund-δ line (e.g. Peeters et al. 2024), and is more strongly affected by contamination by starlight. Meanwhile, the F1130W filter is largely unaffected by starlight and also captures a bright feature in a relatively narrow filter.

5. DISCUSSION

We show that PAH emission can be used to predict CO(2-1) emission with ≈ 0.5 dex (i.e., a factor of ≈ 3) scatter at 100 pc resolution in the disks of star-forming galaxies, without requiring any other information. Doing so, one expects an $\approx \pm 0.2$ dex bias in any given prediction due to galaxy-to-galaxy variations in the CO-to-PAH ratio, which correlates with both $\log_{10} {\rm SFR}/M_\star$ and $\log_{10} M_\star$. We provide prescriptions to account for these galaxy-to-galaxy variations, which can sharpen the prediction even more. Fig. 4 shows an example of such a prediction for the nearby spiral NGC 2903.

Our results formally apply to regions where molecular gas is likely to constitute a significant fraction of the ISM, with $\Sigma_{\rm mol} \gtrsim 4$ M$_\odot$ pc^{-2}. It is likely that in fainter regions the PAH emission reflects the distribution of atomic gas (see Sandstrom et al. 2023a), but the details of that correlation remain less well con-
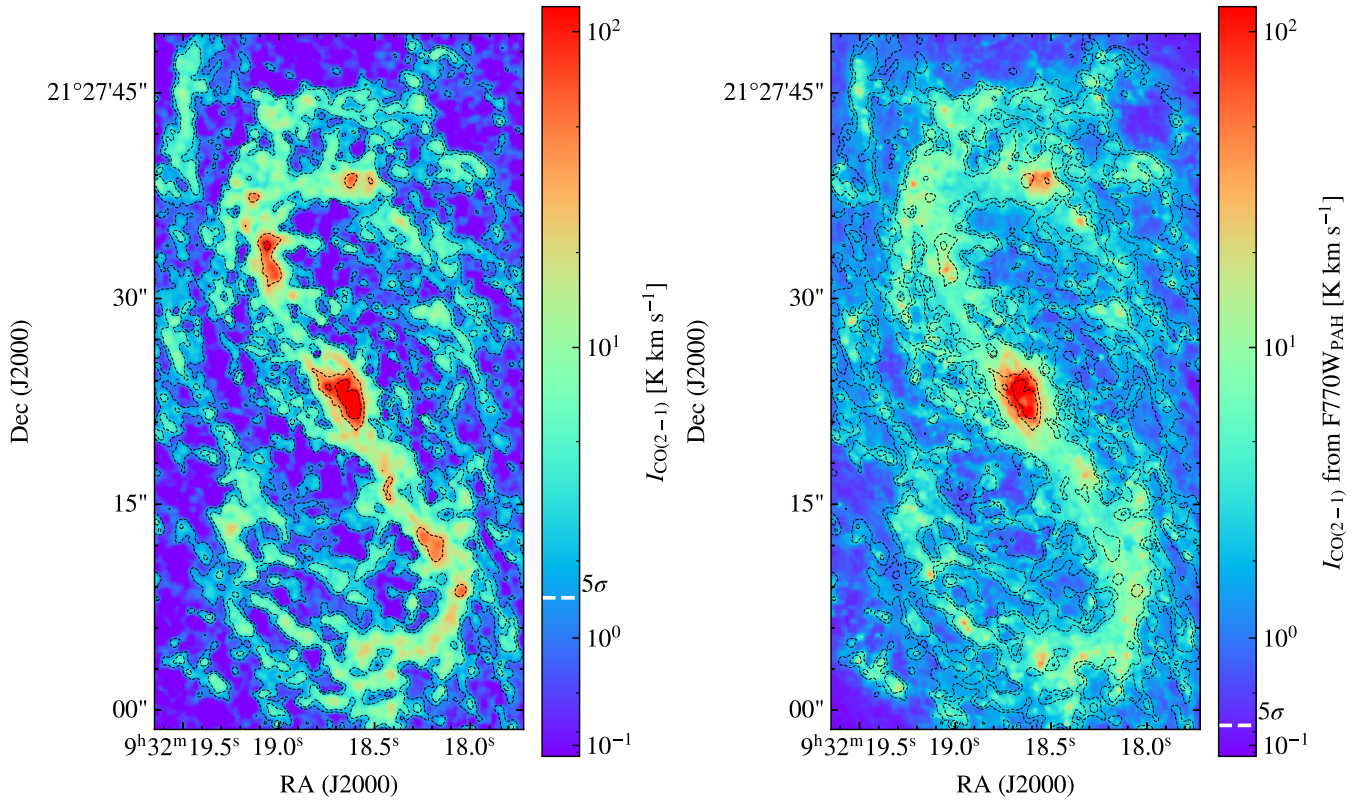
Figure 4. CO and PAH emission in one nearby galaxy. The left panel shows an inclination-corrected ALMA CO(2-1) image of NGC 2903 with contours at 1.25, 3.1, 31, and 100 K km s^{-1}. The right panel shows a predicted CO(2-1) intensity map based on JWST F770W$_{\rm PAH}$ and the prescription in Eq. 5. The contours are the same as on the left panel, and they show a very close correspondence between CO and PAH emission. At the same time, CO(2-1) emission is underestimated in the bar ends, highlighting improvements to be explored in future work. This figure also shows the improved sensitivity of JWST compared to ALMA at recovering faint emission, with the 5σ RMS noise indicated on each colorbar.

strained, including the dependence of PAH abundance on H I phase and density (Hensley et al. 2022). We also emphasize that our results offer a way to predict CO emission, specifically CO(2-1) emission for regions with $I_{\rm F770W}^{\rm PAH} > 0.5$ MJy sr^{-1}. The CO(2-1)-to-H$_2$ conversion factor is known to vary as a function of environment across galaxies and this will need to be included to predict the gas column density, $N({\rm H}_2)$ (e.g., see reviews in Bolatto et al. 2013; Schinnerer & Leroy 2024).

Despite these limitations, the CO-PAH correlation represents a powerful tool. In a matter of minutes on the source, JWST can produce maps with resolution and gas column sensitivity that would take ALMA many hours to match (of course ALMA carries kinematic information and CO represents a well-calibrated gas tracer, so the two remain complementary). As an example of the applications of such data, Pathak et al. (2024) analyzed 19 of the same galaxies we study to infer column density probability distribution functions at high physical resolution, suitable for benchmarking simulations and infer-

ring some aspects of interstellar turbulence and galactic dynamics (Meidt et al. 2023; Thilker et al. 2023).

While the practical applications of the observed correlation are exciting, the stability of the CO-to-PAH ratio across a wide range of systems may reflect that the terms in Eq. 1 have counter-balancing environmental dependencies. The interstellar radiation field varies within and among galaxies (e.g., Draine et al. 2007; Aniano et al. 2020, Chastenet et al. 2024, accepted), as does $X_{\rm CO}$, and $q_{\rm PAH}$ appears strongly suppressed within H II regions (Chastenet et al. 2023a; Egorov et al. 2023; Sutter et al. 2024). This might reflect that environmental effects are somewhat offset, e.g., because U is higher where $R_{\rm PAH}$ (Egorov et al. 2023), as well as $q_{\rm PAH}$ and $\alpha_{\rm CO}$ tend to be low. Alternatively, they might reflect that the emitting PAHs tend to reside predominantly in neutral, moderately shielded gas, subjecting them to some of the same selection effects that apply to CO.

Beyond speculation, having established the basic observational correlations, the clear next step in this area is to follow up with a physically oriented analysis. The

full PHANGS data sets make it possible to combine 21-cm data on atomic gas and best-estimate α_{CO} with estimates of the local interstellar radiation field, U, and PAH abundance, q_{PAH}, to test the physical expectation that $I_{PAH}/N(H) \propto U q_{PAH}^{-1}$. This will both illuminate the reasons for the tightness of the PAH-CO correlation and sharpen the use of PAH emission as an ISM tracer, particularly in the atomic gas-dominated parts of galaxies.

6. CONCLUSIONS

We characterize the relationship between CO(2-1) and near- and mid-infrared (NIR and MIR) PAH emission at ≈ 100 pc scales for 66 nearby ($D \lesssim 20$ Mpc) star-forming galaxies observed as part of PHANGS–ALMA and the PHANGS–JWST Cycle 1 and Cycle 2 treasuries. This is by far the largest comparison of molecular gas tracers and PAH emission at cloud scales to date, more than $10\times$ larger than initial JWST studies. We find:

1. CO(2-1) exhibits strong correlations with the PAH emission captured by JWST's F770W, F335M, and F1130W filters. In regions of galaxies where molecular gas is likely to make up most of the ISM ($I_{F770W} > 0.5$ MJy sr^{-1}; $\Sigma_{mol} \gtrsim 4$ M$_\odot$ pc^{-2}), this correlation appears approximately linear ($0.8 \lesssim m \lesssim 1.2$) and covers more than two orders of magnitude in PAH and CO intensities. We provide power law scaling relations that can be used to predict CO(2-1) from PAH emission (Table 2, Figure 1). The typical sightline-to-sightline scatter about these relations considering the whole sample together is $\sigma \approx 0.5$ dex, and is dominated by statistical noise in the CO measurements in our data set.

2. Subdividing the 19 JWST Cycle 1 targets into sightlines near H II regions and diffuse sightlines, we find overall similar scaling relationships between CO(2-1) and I_{F770}^{PAH} between the two types of regions (Table 2, Figure 1). The main difference appears to be that the nebular regions harbor more high-intensity sightlines than the diffuse regions (see also Pathak et al. 2024). This is consistent with the idea that the nebular regions still contain some well-shielded, denser gas outside the actual H II regions that harbor both CO and PAH molecules (see also Sutter et al. 2024).

3. We also contrast galaxy centers with emission from the surrounding disks, finding that galaxy centers exhibit on average an ≈ 0.2 dex ($\approx 60\%$) higher ratio of CO(2-1)-to-F770W emission compared to galaxy disks (in addition to being brighter in both tracers, as in Pathak et al. 2024). This might reflect that the enhanced CO emission (i.e., low α_{CO}) in galaxy centers (e.g., Teng et al. 2023; Chiang et al. 2024) represents a stronger effect than any enhancement in PAH emission due to a more intense interstellar radiation field. Because of this contrast, when fitting emission from both disk and central regions, the slope of the CO vs. PAH relation tends to be somewhat steeper than what we observe for disks or centers alone.

4. Individual galaxies show similar relations between CO(2-1) and PAH intensity, but with $\approx \pm 0.2$ dex scatter in the normalization. The ratio of CO at fixed PAH intensity for a galaxy correlates with its stellar mass, $M_\star$, and anti-correlates with its specific star formation rate SFR/$M_\star$, in good agreement with results for integrated galaxies using WISE. We provide prescriptions to predict resolved CO emission from PAH emission that also take into account galaxy-dependent normalizations and these represent our best overall predictor.

5. We also present scaling relations and observe strong correlations linking CO(2-1) and emission in the PAH-dominated F1130W filter as well as continuum-subtracted F335M$_{PAH}$ emission. The F1130W band has coarser resolution but is least affected by starlight contamination out of the three PAH-tracing bands we consider. The fainter F335M$_{PAH}$ emission offers the prospect of tracing CO at thie highest resolution but depends sensitively on stellar continuum subtraction (H. Koziol et al. in preparation; Sandstrom et al. 2023b; Bolatto et al. 2024).

7. ACKNOWLEDGMENTS

Facilities: JWST, ALMA, VLT/MUSE

Software: astropy (Astropy Collaboration et al. 2018)

APPENDIX

A. FITS FOR INDIVIDUAL GALAXIES

Table 3 shows the best-fit parameters of the CO(2-1) vs. F335M$_{\rm PAH}$, F770W$_{\rm PAH}$, and F1130W relationships for each galaxy. We also report the stellar mass and SFR/$M_\star$, adopted from Leroy et al. (2019), the brightness of band X in that galaxy at $I_\nu^X = 1$ MJy sr^{-1}, the number of sight lines analyzed, and Spearman's rank correlation coefficient relating the PAH and CO emission for each sightline.

Table 3. Fits to all pixels outside galaxy centers for each galaxy.

Name	Cycle	$\log_{10} M_\star$	$\log_{10} \mathrm{SFR}/M_\star$	m	b	x_0	$\log_{10} C_{\mathrm{band}}$	N_{pix}	r
				$I_{\mathrm{CO(2-1)}}$ vs F770W$_{\mathrm{PAH}}$					
IC5273	2	9.72	−9.99	0.941 ± 0.215	0.217 ± 0.090	0.517	−0.269	19065	0.68
IC5332	1	9.68	−10.07	0.415 ± 0.866	0.352 ± 0.270	0.375	0.197	6748	0.18
NGC0628	1	10.34	−10.10	0.697 ± 0.294	0.591 ± 0.116	0.517	0.231	11989	0.54
NGC1087	1	9.94	−9.83	1.174 ± 0.188	0.614 ± 0.102	0.801	−0.326	9201	0.72
NGC1097	2	10.76	−10.08	0.755 ± 0.213	0.674 ± 0.097	0.588	0.230	55013	0.61
NGC1300	1	10.62	−10.55	0.897 ± 0.492	0.508 ± 0.169	0.446	0.109	3665	0.46
NGC1365	1	11.00	−9.76	1.299 ± 0.335	0.803 ± 0.178	0.588	0.040	9512	0.39
NGC1385	1	9.98	−9.66	1.034 ± 0.175	0.584 ± 0.112	0.872	−0.318	10653	0.74
NGC1433	1	10.87	−10.82	1.248 ± 0.501	0.576 ± 0.165	0.446	0.020	6738	0.40
NGC1511	2	9.91	−9.55	0.895 ± 0.117	0.559 ± 0.068	0.801	−0.158	14424	0.82
NGC1512	1	10.72	−10.61	0.900 ± 0.623	0.377 ± 0.160	0.304	0.104	3243	0.48
NGC1546	2	10.35	−10.43	0.824 ± 0.092	0.753 ± 0.044	0.659	0.210	9933	0.96
NGC1559	2	10.36	−9.79	0.947 ± 0.150	0.519 ± 0.083	0.801	−0.239	42127	0.76
NGC1566	1	10.79	−10.13	1.003 ± 0.192	0.826 ± 0.121	0.872	−0.048	28064	0.60
NGC1637	2	9.95	−10.14	0.791 ± 0.223	0.548 ± 0.092	0.588	0.083	39895	0.67
NGC1672	1	10.73	−9.85	1.239 ± 0.263	0.733 ± 0.128	0.730	−0.170	8946	0.64
NGC1792	2	10.61	−10.04	0.852 ± 0.115	0.780 ± 0.068	0.872	0.037	59996	0.86
NGC1809	2	9.77	−9.01	0.977 ± 0.440	0.230 ± 0.130	0.375	−0.136	6042	0.58
NGC2090	2	10.04	−10.43	0.639 ± 0.325	0.392 ± 0.108	0.375	0.153	13045	0.66
NGC2283	2	9.89	−10.17	0.948 ± 0.258	0.289 ± 0.108	0.588	−0.269	26689	0.58
NGC2566	2	10.71	−9.77	0.907 ± 0.293	0.611 ± 0.122	0.588	0.078	34275	0.56
NGC2775	2	11.07	−11.13	0.694 ± 0.300	0.492 ± 0.094	0.375	0.232	26633	0.56
NGC2835	1	10.00	−9.90	0.936 ± 0.424	0.380 ± 0.161	0.517	−0.104	10158	0.39
NGC2903	2	10.63	−10.15	0.844 ± 0.136	0.709 ± 0.083	0.801	0.034	119478	0.74
NGC2997	2	10.73	−10.09	0.773 ± 0.115	0.864 ± 0.077	0.943	0.135	223223	0.67
NGC3059	2	10.38	−10.00	1.014 ± 0.107	0.934 ± 0.078	1.085	−0.167	59783	0.66
NGC3137	2	9.88	−10.19	0.574 ± 1.485	0.140 ± 0.294	0.233	0.006	4403	0.51
NGC3239	2	9.17	−9.58	0.932 ± 0.793	-0.047 ± 0.231	0.304	−0.330	1257	0.33
NGC3351	1	10.37	−10.25	0.424 ± 1.204	0.356 ± 0.332	0.304	0.227	7080	0.24
NGC3507	2	10.40	−10.40	0.838 ± 0.267	0.503 ± 0.109	0.517	0.070	30466	0.54
NGC3511	2	10.03	−10.12	0.974 ± 0.246	0.366 ± 0.091	0.446	−0.068	19751	0.75
NGC3521	2	11.02	−10.45	0.976 ± 0.135	0.648 ± 0.073	0.730	−0.065	103581	0.88
NGC3596	2	9.66	−10.18	0.785 ± 0.192	0.650 ± 0.090	0.659	0.133	21993	0.69
NGC3621	2	10.06	−10.06	1.010 ± 0.128	0.654 ± 0.073	0.801	−0.155	97443	0.76
NGC3626	2	10.46	−11.13	0.794 ± 0.377	0.475 ± 0.121	0.446	0.122	3168	0.75
NGC3627	1	10.84	−10.25	1.014 ± 0.169	0.863 ± 0.111	0.872	−0.020	24320	0.75

Table 3 *continued*

Table 3 *(continued)*

Name	Cycle	$\log_{10} M_\star$	$\log_{10} \mathrm{SFR}/M_\star$	m	b	x_0	$\log_{10} C_{\mathrm{band}}$	N_{pix}	r
NGC4254	1	10.42	−9.93	1.145 ± 0.204	0.703 ± 0.108	0.730	−0.132	20130	0.81
NGC4298	2	10.02	−10.36	0.624 ± 0.173	0.586 ± 0.070	0.517	0.264	25588	0.75
NGC4303	1	10.51	−9.78	0.964 ± 0.209	0.703 ± 0.120	0.801	−0.068	16580	0.69
NGC4321	1	10.75	−10.20	1.080 ± 0.215	0.789 ± 0.110	0.659	0.078	26681	0.63
NGC4424	2	9.91	−10.43	1.052 ± 0.178	0.553 ± 0.102	0.801	−0.289	3695	0.59
NGC4457	2	10.42	−10.93	0.565 ± 0.349	0.784 ± 0.145	0.588	0.452	9790	0.40
NGC4496A	2	9.53	−9.74	0.698 ± 0.385	0.273 ± 0.123	0.446	−0.038	8446	0.43
NGC4535	1	10.54	−10.20	1.111 ± 0.325	0.685 ± 0.120	0.517	0.111	8582	0.55
NGC4536	2	10.40	−9.86	1.092 ± 0.144	0.779 ± 0.080	0.730	−0.017	20165	0.69
NGC4540	2	9.79	−10.56	0.819 ± 0.223	0.592 ± 0.105	0.588	0.111	11515	0.56
NGC4548	2	10.69	−10.97	0.794 ± 0.329	0.562 ± 0.122	0.446	0.208	11678	0.51
NGC4569	2	10.81	−10.68	0.720 ± 0.127	0.804 ± 0.066	0.659	0.330	23275	0.62
NGC4571	2	10.09	−10.63	0.466 ± 0.349	0.410 ± 0.113	0.375	0.235	16364	0.28
NGC4579	2	11.15	−10.81	0.674 ± 0.186	0.726 ± 0.092	0.659	0.283	40074	0.54
NGC4654	2	10.57	−9.99	0.895 ± 0.110	0.835 ± 0.069	0.872	0.055	52112	0.80
NGC4689	2	10.22	−10.61	0.756 ± 0.227	0.651 ± 0.088	0.517	0.261	32495	0.65
NGC4694	2	9.86	−10.66	0.979 ± 0.156	0.458 ± 0.079	0.659	−0.188	1860	0.55
NGC4731	2	9.48	−9.70	0.715 ± 0.235	0.199 ± 0.090	0.517	−0.170	4385	0.52
NGC4781	2	9.64	−9.96	0.955 ± 0.155	0.434 ± 0.073	0.659	−0.195	27874	0.81
NGC4826	2	10.24	−10.93	0.798 ± 0.139	0.970 ± 0.083	0.872	0.274	20907	0.84
NGC4941	2	10.17	−10.53	0.290 ± 1.000	0.187 ± 0.222	0.233	0.120	4679	0.24
NGC4951	2	9.79	−10.24	0.974 ± 0.386	0.250 ± 0.124	0.375	−0.115	5225	0.65
NGC5042	2	9.90	−10.12	0.833 ± 0.504	0.219 ± 0.153	0.375	−0.093	12488	0.42
NGC5068	1	9.41	−9.97	0.919 ± 0.625	0.373 ± 0.243	0.517	−0.102	12231	0.35
NGC5134	2	10.41	−10.75	0.744 ± 0.290	0.423 ± 0.119	0.517	0.038	15980	0.51
NGC5248	2	10.41	−10.05	0.926 ± 0.150	0.832 ± 0.080	0.801	0.091	63197	0.78
NGC5643	2	10.34	−9.92	0.769 ± 0.161	0.698 ± 0.098	0.801	0.083	99320	0.67
NGC6300	2	10.47	−10.19	0.840 ± 0.194	0.731 ± 0.087	0.730	0.117	67368	0.66
NGC7456	2	9.64	−10.08	0.636 ± 0.067	-0.179 ± 0.002	0.090	−0.237	922	0.19
NGC7496	1	10.00	−9.65	0.985 ± 0.352	0.371 ± 0.126	0.446	−0.069	4023	0.59

$I_{\mathrm{CO(2-1)}}$ vs F335M$_{\mathrm{PAH}}$

Name	Cycle	$\log_{10} M_\star$	$\log_{10} \mathrm{SFR}/M_\star$	m	b	x_0	$\log_{10} C_{\mathrm{band}}$	N_{pix}	r
IC5332	1	9.68	−10.07	0.266 ± 3.333	0.380 ± 0.596	−0.700	0.566	1307	0.11
NGC0628	1	10.34	−10.10	0.445 ± 0.294	0.741 ± 0.095	−0.500	0.963	2616	0.34
NGC1087	1	9.94	−9.83	1.218 ± 0.214	0.721 ± 0.079	−0.300	1.086	6412	0.73
NGC1300	1	10.62	−10.55	0.938 ± 0.607	0.720 ± 0.138	−0.600	1.283	596	0.44
NGC1365	1	11.00	−9.76	1.000 ± 0.768	0.721 ± 0.184	−0.550	1.271	1335	0.26
NGC1385	1	9.98	−9.66	0.942 ± 0.123	0.825 ± 0.059	−0.150	0.966	5778	0.75
NGC1433	1	10.87	−10.82	0.854 ± 0.974	0.574 ± 0.195	−0.650	1.130	1160	0.42
NGC1512	1	10.72	−10.61	0.776 ± 1.698	0.507 ± 0.276	−0.700	1.050	624	0.43
NGC1566	1	10.79	−10.13	0.807 ± 0.172	1.085 ± 0.093	−0.150	1.206	7885	0.52

Table 3 *continued*

Chown et al.

Table 3 (continued)

Name	Cycle	$\log_{10} M_\star$	$\log_{10} \text{SFR}/M_\star$	m	b	x_0	$\log_{10} C_{\text{band}}$	N_{pix}	r
NGC1672	1	10.73	−9.85	0.988 ± 0.362	0.874 ± 0.121	−0.400	1.269	3014	0.50
NGC2835	1	10.00	−9.90	0.704 ± 0.379	0.579 ± 0.108	−0.500	0.932	1475	0.46
NGC3351	1	10.37	−10.25	-0.121 ± 126.184	0.282 ± 24.668	−0.750	0.191	452	0.14
NGC3627	1	10.84	−10.25	1.019 ± 0.157	1.088 ± 0.083	−0.150	1.241	18505	0.66
NGC4254	1	10.42	−9.93	0.826 ± 0.150	1.092 ± 0.071	−0.250	1.299	10263	0.68
NGC4303	1	10.51	−9.78	0.546 ± 0.142	1.109 ± 0.070	−0.250	1.246	2285	0.54
NGC4321	1	10.75	−10.20	0.833 ± 0.192	1.088 ± 0.071	−0.350	1.379	2621	0.55
NGC4535	1	10.54	−10.20	0.826 ± 0.471	0.881 ± 0.118	−0.550	1.336	1118	0.45
NGC5068	1	9.41	−9.97	0.913 ± 0.459	0.539 ± 0.146	−0.450	0.950	4319	0.37
NGC7496	1	10.00	−9.65	0.773 ± 0.423	0.557 ± 0.110	−0.550	0.982	797	0.44

$I_{\text{CO}(2-1)}$ vs F1130W

Name	Cycle	$\log_{10} M_\star$	$\log_{10} \text{SFR}/M_\star$	m	b	x_0	$\log_{10} C_{\text{band}}$	N_{pix}	r
IC5332	1	9.68	−10.07	0.456 ± 1.076	0.341 ± 0.265	0.387	0.165	9230	0.20
NGC0628	1	10.34	−10.10	0.768 ± 0.258	0.540 ± 0.107	0.624	0.060	13252	0.58
NGC1087	1	9.94	−9.83	1.216 ± 0.194	0.504 ± 0.091	0.862	−0.544	9792	0.75
NGC1300	1	10.62	−10.55	0.873 ± 0.368	0.492 ± 0.133	0.565	−0.001	4496	0.48
NGC1365	1	11.00	−9.76	1.431 ± 0.307	0.758 ± 0.157	0.743	−0.305	11519	0.49
NGC1385	1	9.98	−9.66	1.055 ± 0.158	0.542 ± 0.099	0.981	−0.492	11230	0.76
NGC1433	1	10.87	−10.82	1.209 ± 0.299	0.544 ± 0.120	0.624	−0.211	9508	0.44
NGC1512	1	10.72	−10.61	0.913 ± 0.409	0.342 ± 0.120	0.446	−0.066	4395	0.47
NGC1566	1	10.79	−10.13	1.023 ± 0.195	0.775 ± 0.131	0.981	−0.229	31090	0.61
NGC1672	1	10.73	−9.85	1.284 ± 0.254	0.604 ± 0.132	0.803	−0.427	9569	0.67
NGC2835	1	10.00	−9.90	0.892 ± 0.383	0.351 ± 0.148	0.624	−0.206	12212	0.42
NGC3351	1	10.37	−10.25	0.376 ± 0.739	0.269 ± 0.207	0.446	0.101	9418	0.26
NGC3627	1	10.84	−10.25	1.157 ± 0.152	0.831 ± 0.089	1.040	−0.373	24603	0.76
NGC4254	1	10.42	−9.93	1.161 ± 0.165	0.671 ± 0.091	0.862	−0.329	20433	0.83
NGC4303	1	10.51	−9.78	0.986 ± 0.179	0.669 ± 0.112	0.921	−0.240	16929	0.74
NGC4321	1	10.75	−10.20	1.140 ± 0.244	0.699 ± 0.109	0.743	−0.149	28405	0.69
NGC4535	1	10.54	−10.20	1.021 ± 0.257	0.640 ± 0.102	0.624	0.002	10486	0.57
NGC5068	1	9.41	−9.97	0.941 ± 0.615	0.342 ± 0.256	0.624	−0.246	14081	0.36
NGC7496	1	10.00	−9.65	1.051 ± 0.261	0.333 ± 0.098	0.565	−0.260	4541	0.64

Note— Columns: Cycle — Indicates whether the galaxy was observed as part of Cycle 1 (GO 2107) or Cycle 2 (GO 3707); $\log_{10} M_\star$ — global stellar mass [$M_\odot$]; $\log_{10} \text{SFR}/M_\star$ global specific star formation rate [yr^{-1}]; m, b, x_0 — best fit power law scaling parameters following Equation 2 relating CO(2-1) to intensity in band X; C_{band} — the normalization of the best-fit relation at $I_\nu^X = 1$ MJy sr^{-1} [K km s^{-1} (MJy sr^{-1})$^{-1}$]; N_{pix} — number of sight lines entering the analysis, where approximately four sight lines correspond to one independent measurements; r — rank correlation between CO(2-1) and intensity in band X for all sight lines.

B. HOW TO ESTIMATE CO (2-1) INTENSITY FROM PAH EMISSION MAPS

We suggest the following recipe, along with some key caveats, to estimate CO (2-1) intensity in units of K km s^{-1} from JWST observations of PAH-dominated filters in units of MJy sr^{-1}.

1. In the case of F335M or F770W, estimate and subtract the associate stellar continuum to calculate $I_{\rm F335M}^{\rm PAH}$ or $I_{\rm F770W}^{\rm PAH}$. Specifically, subtract $0.22 \times I_{\rm F300M}$ or $0.13 \times I_{\rm F200W}$ from $I_{\rm F770W}$ (see §3.1 and Sutter et al. 2024). If this is not possible, we view F335M as not useful, while F770W can be used with our provided equations but will be biased high in regions of high stellar-to-dust ratios, including stellar bars and bulges. We do not consider stellar continuum correction necessary for F1130W.

2. For a disk galaxy with inclination i, correct the surface brightness by multiplying by $\cos i$.

3. If the specific star formation rate, SFR/$M_\star$, is known (e.g. from Leroy et al. 2019) and the galaxy resembles a low redshift star-forming galaxy (so that our corrections could be expected to apply), evaluate Equation 3 to obtain $C_{\rm norm}^{\rm F770W}$. We prefer the SFR/$M_\star$ based correction. For F335M$_{\rm PAH}$ and F1130W, we recommend multiplying $C_{\rm F770W}^{\rm PAH}$ (top right panel of Figure 2) by typical band ratios F335M$_{\rm PAH}$/F770W$_{\rm PAH}$ ≈ 0.04 or F1130W/F770W$_{\rm PAH}$ ≈ 0.69 (using x_0 from Table 2) to yield $C_{\rm F335M}^{\rm PAH}$ and $C_{\rm F1130W}$ respectively. If this is step is not possible, one can make a less accurate estimate by applying the general relation (i.e., simply use the appropriate equation from Table 2 and ignore the following step).In this case, one should expect ≈ 0.2 dex bias in the predicted CO (2-1) map for any individual galaxy.

4. If $\log_{10} C_{\rm norm}$ has been estimated, subtract this from the observed $\log_{10} I_{\rm F770W}^{\rm PAH}$ for each sight line to remove the galaxy-to-galaxy normalization. Then for F770W$_{\rm PAH}$, plug this normalized intensity, x, into Equation 5 to estimate $y \equiv \log_{10} I_{\rm CO(2-1)}$. For F335M$_{\rm PAH}$,

$$y = (1.02 \pm 0.08)(x - 0.05) + (0.21 \pm 0.07), \tag{B1}$$

where x and y are defined as in Equation 5 and the full Cycle 1 data set shows 0.45 dex rms scatter in the residuals. Similarly for F1130W, we find

$$y = (1.05 \pm 0.08)(x - 1.28) + (1.43 \pm 0.06). \tag{B2}$$

This procedure will predict the CO (2-1) intensity. In many cases the molecular gas mass will be the quantity of direct interest. In future work, we aim to explore how $I_{\rm F770W}^{\rm PAH}$ compares to $N(H)$ directly. For now, to convert from CO intensity to molecular gas column or surface density, one should multiply the predicted CO maps by an appropriate CO (2-1)-to-H$_2$ conversion factor. Bolatto et al. (2013) review the CO-to-H$_2$ conversion factor and Schinnerer & Leroy (2024) provide current prescriptions that attempt to account for variations in opacity, CO excitation, and metallicity.

REFERENCES

Allamandola, L. J., Tielens, A. G. G. M., & Barker, J. R. 1989, ApJS, 71, 733, doi: 10.1086/191396

Aniano, G., Draine, B. T., Gordon, K. D., & Sandstrom, K. 2011, PASP, 123, 1218, doi: 10.1086/662219

Aniano, G., Draine, B. T., Hunt, L. K., et al. 2020, ApJ, 889, 150, doi: 10.3847/1538-4357/ab5fdb

Astropy Collaboration, Price-Whelan, A. M., Sipőcz, B. M., et al. 2018, AJ, 156, 123, doi: 10.3847/1538-3881/aabc4f

Barnes, A. T., Chandar, R., Kreckel, K., et al. 2022, A&A, 662, L6, doi: 10.1051/0004-6361/202243766

Baron, D., Sandstrom, K. M., Rosolowsky, E., et al. 2024, ApJ, 968, 24, doi: 10.3847/1538-4357/ad39e5

Belfiore, F., Leroy, A. K., Williams, T. G., et al. 2023, arXiv e-prints, arXiv:2306.11811, doi: 10.48550/arXiv.2306.11811

Bolatto, A. D., Wolfire, M., & Leroy, A. K. 2013, ARA&A, 51, 207, doi: 10.1146/annurev-astro-082812-140944

Bolatto, A. D., Levy, R. C., Tarantino, E., et al. 2024, ApJ, 967, 63, doi: 10.3847/1538-4357/ad33c8

Boulanger, F., & Perault, M. 1988, ApJ, 330, 964, doi: 10.1086/166526

Calzetti, D., Kennicutt, R. C., Engelbracht, C. W., et al. 2007, ApJ, 666, 870, doi: 10.1086/520082

Chastenet, J., Sutter, J., Sandstrom, K., et al. 2023a, ApJL, 944, L12, doi: 10.3847/2041-8213/acac94

—. 2023b, ApJL, 944, L11, doi: 10.3847/2041-8213/acadd7

Chiang, I.-D., Sandstrom, K. M., Chastenet, J., et al. 2024, ApJ, 964, 18, doi: 10.3847/1538-4357/ad23ed

Chown, R., Li, C., Parker, L., et al. 2021, MNRAS, 500, 1261, doi: 10.1093/mnras/staa3288

Chown, R., Sidhu, A., Peeters, E., et al. 2024, A&A, 685, A75, doi: 10.1051/0004-6361/202346662

Compiègne, M., Abergel, A., Verstraete, L., & Habart, E. 2008, A&A, 491, 797, doi: 10.1051/0004-6361:200809850

Compiègne, M., Flagey, N., Noriega-Crespo, A., et al. 2010, ApJL, 724, L44, doi: 10.1088/2041-8205/724/1/L44

Doré, O., Werner, M. W., Ashby, M. L. N., et al. 2018, arXiv e-prints, arXiv:1805.05489, doi: 10.48550/arXiv.1805.05489

Draine, B. T. 2011, Physics of the Interstellar and Intergalactic Medium

Draine, B. T., & Li, A. 2007, ApJ, 657, 810, doi: 10.1086/511055

Draine, B. T., Li, A., Hensley, B. S., et al. 2021, ApJ, 917, 3, doi: 10.3847/1538-4357/abff51

Draine, B. T., Dale, D. A., Bendo, G., et al. 2007, ApJ, 663, 866, doi: 10.1086/518306

Egorov, O. V., Kreckel, K., Sandstrom, K. M., et al. 2023, ApJL, 944, L16, doi: 10.3847/2041-8213/acac92

Emsellem, E., Schinnerer, E., Santoro, F., et al. 2022, A&A, 659, A191, doi: 10.1051/0004-6361/202141727

Galliano, F., Galametz, M., & Jones, A. P. 2018, ARA&A, 56, 673, doi: 10.1146/annurev-astro-081817-051900

Gao, Y., Tan, Q.-H., Gao, Y., et al. 2022, arXiv e-prints, arXiv:2210.01982. https://arxiv.org/abs/2210.01982

Gao, Y., Xiao, T., Li, C., et al. 2019, ApJ, 887, 172, doi: 10.3847/1538-4357/ab557c

Gordon, K. D., Engelbracht, C. W., Rieke, G. H., et al. 2008, ApJ, 682, 336, doi: 10.1086/589567

Groves, B., Kreckel, K., Santoro, F., et al. 2023, MNRAS, 520, 4902, doi: 10.1093/mnras/stad114

Hensley, B. S., Murray, C. E., & Dodici, M. 2022, ApJ, 929, 23, doi: 10.3847/1538-4357/ac5cbd

Israel, F. P. 2020, A&A, 635, A131, doi: 10.1051/0004-6361/201834198

Kelly, B. C. 2007, ApJ, 665, 1489, doi: 10.1086/519947

Kennicutt, R. C., & Evans, N. J. 2012, ARA&A, 50, 531, doi: 10.1146/annurev-astro-081811-125610

Lang, P., Meidt, S. E., Rosolowsky, E., et al. 2020, ApJ, 897, 122, doi: 10.3847/1538-4357/ab9953

Lebouteiller, V., Brandl, B., Bernard-Salas, J., Devost, D., & Houck, J. R. 2007, ApJ, 665, 390, doi: 10.1086/519014

Lee, J. C., Sandstrom, K. M., Leroy, A. K., et al. 2023, ApJL, 944, L17, doi: 10.3847/2041-8213/acaaae

Leger, A., & Puget, J. L. 1984, A&A, 137, L5

Leroy, A. K., Sandstrom, K. M., Lang, D., et al. 2019, ApJS, 244, 24, doi: 10.3847/1538-4365/ab3925

Leroy, A. K., Schinnerer, E., Hughes, A., et al. 2021, ApJS, 257, 43, doi: 10.3847/1538-4365/ac17f3

Leroy, A. K., Bolatto, A. D., Sandstrom, K., et al. 2023a, ApJL, 944, L10, doi: 10.3847/2041-8213/acab01

Leroy, A. K., Sandstrom, K., Rosolowsky, E., et al. 2023b, ApJL, 944, L9, doi: 10.3847/2041-8213/acaf85

Li, J., Kreckel, K., Sarbadhicary, S., et al. 2024, arXiv e-prints, arXiv:2405.08974, doi: 10.48550/arXiv.2405.08974

Linzer, N. B., Kim, J.-G., Kim, C.-G., & Ostriker, E. C. 2024, arXiv e-prints, arXiv:2409.05958, doi: 10.48550/arXiv.2409.05958

Madden, S. C., Galliano, F., Jones, A. P., & Sauvage, M. 2006, A&A, 446, 877, doi: 10.1051/0004-6361:20053890

Maragkoudakis, A., Peeters, E., & Ricca, A. 2020, MNRAS, 494, 642, doi: 10.1093/mnras/staa681

Meidt, S. E., Rosolowsky, E., Sun, J., et al. 2023, ApJL, 944, L18, doi: 10.3847/2041-8213/acaaa8

Montillaud, J., Joblin, C., & Toublanc, D. 2013, A&A, 552, A15, doi: 10.1051/0004-6361/201220757

Neumann, L., den Brok, J. S., Bigiel, F., et al. 2023, A&A, 675, A104, doi: 10.1051/0004-6361/202346129

Pathak, D., Leroy, A. K., Thompson, T. A., et al. 2024, AJ, 167, 39, doi: 10.3847/1538-3881/ad110d

Pedrini, A., Adamo, A., Calzetti, D., et al. 2024, arXiv e-prints, arXiv:2406.01666, doi: 10.48550/arXiv.2406.01666

Peeters, E., Spoon, H. W. W., & Tielens, A. G. G. M. 2004, ApJ, 613, 986, doi: 10.1086/423237

Peeters, E., Habart, E., Berné, O., et al. 2024, A&A, 685, A74, doi: 10.1051/0004-6361/202348244

Pety, J., Teyssier, D., Fossé, D., et al. 2005, A&A, 435, 885, doi: 10.1051/0004-6361:20041170

Povich, M. S., Stone, J. M., Churchwell, E., et al. 2007, ApJ, 660, 346, doi: 10.1086/513073

Puget, J. L., & Leger, A. 1989, ARA&A, 27, 161, doi: 10.1146/annurev.aa.27.090189.001113

Querejeta, M., Schinnerer, E., Meidt, S., et al. 2021, A&A, 656, A133, doi: 10.1051/0004-6361/202140695

Regan, M. W., Thornley, M. D., Bendo, G. J., et al. 2004, ApJS, 154, 204, doi: 10.1086/423204

Saintonge, A., & Catinella, B. 2022, arXiv e-prints, arXiv:2202.00690. https://arxiv.org/abs/2202.00690

Saintonge, A., Catinella, B., Tacconi, L. J., et al. 2017, ApJS, 233, 22, doi: 10.3847/1538-4365/aa97e0

Sandstrom, K. M., Leroy, A. K., Walter, F., et al. 2013, ApJ, 777, 5, doi: 10.1088/0004-637X/777/1/5

Sandstrom, K. M., Koch, E. W., Leroy, A. K., et al. 2023a, ApJL, 944, L8, doi: 10.3847/2041-8213/aca972

Sandstrom, K. M., Chastenet, J., Sutter, J., et al. 2023b, ApJL, 944, L7, doi: 10.3847/2041-8213/acb0cf

Santoro, F., Kreckel, K., Belfiore, F., et al. 2022, A&A, 658, A188, doi: 10.1051/0004-6361/202141907

Schinnerer, E., & Leroy, A. K. 2024, arXiv e-prints, arXiv:2403.19843, doi: 10.48550/arXiv.2403.19843

Schinnerer, E., Emsellem, E., Henshaw, J. D., et al. 2023, ApJL, 944, L15, doi: 10.3847/2041-8213/acac9e

Smith, J. D. T., Draine, B. T., Dale, D. A., et al. 2007, ApJ, 656, 770, doi: 10.1086/510549

Sun, J., Leroy, A. K., Ostriker, E. C., et al. 2020, ApJ, 892, 148, doi: 10.3847/1538-4357/ab781c

Sutter, J., Sandstrom, K., Chastenet, J., et al. 2024, arXiv e-prints, arXiv:2405.15102, doi: 10.48550/arXiv.2405.15102

Teng, Y.-H., Sandstrom, K. M., Sun, J., et al. 2023, ApJ, 950, 119, doi: 10.3847/1538-4357/accb86

Thilker, D. A., Lee, J. C., Deger, S., et al. 2023, ApJL, 944, L13, doi: 10.3847/2041-8213/acaeac

Tielens, A. G. G. M. 2008, ARA&A, 46, 289, doi: 10.1146/annurev.astro.46.060407.145211

Whitcomb, C. M., Sandstrom, K., Leroy, A., & Smith, J. D. T. 2023a, ApJ, 948, 88, doi: 10.3847/1538-4357/acc316

Whitcomb, C. M., Sandstrom, K., & Smith, J.-D. T. 2023b, Research Notes of the American Astronomical Society, 7, 38, doi: 10.3847/2515-5172/acc073

Williams, T. G., Lee, J. C., Larson, K. L., et al. 2024, ApJS, 273, 13, doi: 10.3847/1538-4365/ad4be5